Available online at www.sciencedirect.com
SCIENCE DIRECT®
Comput. Methods Appl. Mech. Engrg. 195 (2006) 5115–5140
Computer methods in applied mechanics and engineering
www.elsevier.com/locate/cma

Critical state plasticity. Part VI: Meso-scale finite element simulation of strain localization in discrete granular materials

Ronaldo I. Borja *,[1], José E. Andrade

Department of Civil and Environmental Engineering, Stanford University, Stanford, CA 94305, USA

Received 13 March 2005; received in revised form 30 August 2005; accepted 31 August 2005

Abstract

Development of more accurate mathematical models of discrete granular material behavior requires a fundamental understanding of deformation and strain localization phenomena. This paper utilizes a meso-scale finite element modeling approach to obtain an accurate and thorough capture of deformation and strain localization processes in discrete granular materials such as sands. We employ critical state theory and implement an elastoplastic constitutive model for granular materials, a variant of a model called "Nor-Sand", allowing for non-associative plastic flow and formulating it in the finite deformation regime. Unlike the previous versions of critical state plasticity models presented in a series of "Cam-Clay" papers, the present model contains an additional state parameter ψ that allows for a deviation or detachment of the yield surface from the critical state line. Depending on the sign of this state parameter, the model can reproduce plastic compaction as well as plastic dilation in either loose or dense granular materials. Through numerical examples we demonstrate how a structured spatial density variation affects the predicted strain localization patterns in dense sand specimens.

Keywords: Granular materials; Strain localization

1. Introduction

Development of accurate mathematical models of discrete granular material behavior requires a fundamental understanding of the localization phenomena, such as the formation of shear bands in dense sands. For this reason, much experimental work has been conducted to gain a better understanding of the localization process in these materials [1–11]. The subject also has spurred considerable interest in the theoretical and computational modeling fields [12–29]. It is important to recognize that the material response observed in the laboratory is a result of many different micro-mechanical processes, such as mineral particle rolling and sliding in granular soils, micro-cracking in brittle rocks, and mineral particle rotation and translation in the cement matrix of soft rocks. Ideally, any localization model for geomaterials must represent all of these processes. However, current limitations of experimental and mathematical modeling techniques in capturing the evolution in the micro-scale throughout testing have inhibited the use of a micro-mechanical description of the localized deformation behavior.

To circumvent the problems associated with the micro-mechanical modeling approach, a macro-mechanical approach is often used. For soils, this approach pertains to the specimen being considered as a macro-scale element from which the material response may be inferred. The underlying assumption is that the specimen is prepared uniformly and deformed

* Corresponding author. Fax: +1 650 723 7514.
E-mail address: borja@stanford.edu (R.I. Borja).
[1] Supported by US National Science Foundation, Grant Nos. CMS-0201317 and CMS-0324674.

0045-7825/$ - see front matter
doi:10.1016/j.cma.2005.08.020

homogeneously enough to allow extraction of the material response from the specimen response. However, it is well known that each specimen is unique, and that two identically prepared samples could exhibit different mechanical responses in the regime of instability even if they had been subjected to the same initially homogeneous deformation field. This implies that the size of a specimen is too large to accurately resolve the macro-scale field, and that it can only capture the strain localization phenomena in a very approximate way.

In this paper, we adopt a more refined approach to investigating strain localization phenomena based on a meso-scale description of the granular material behavior. As a matter of terminology, the term "meso-scale" is used in this paper to refer to a scale larger than the grain scale (particle scale) but smaller than the element, or specimen, scale (macro-scale). This approach is motivated primarily by the current advances in laboratory testing capabilities that allow accurate measurements of material imperfection in the specimens, such as X-ray computed tomography (CT) and digital image processing (DIP) in granular soils [1,4,8,9,29]. For example, Fig. 1 shows the result of a CT scan on a biaxial specimen of pure silica sand having a mean grain diameter of 0.5 mm and prepared via air pluviation. The gray level variations in the image indicate differences in the meso-scale local density, with lighter colors indicating regions of higher density (the large white spot in the lower level of the specimen is a piece of gravel). This advanced technology in laboratory testing, combined with DIP to quantitatively transfer the CT results as input into a numerical model, enhances an accurate meso-scale description of granular material behavior and motivates the development of robust meso-scale modeling approaches for replicating the shear banding processes in discrete granular materials.

The modeling approach pursued in this paper utilizes nonlinear continuum mechanics and the finite element method, in combination with a constitutive model based on critical state plasticity that captures both hardening and softening responses depending on the state of the material at yield. The first plasticity model exhibiting such features that comes to mind is the classical modified Cam-Clay [24,30–36]. However, this model may not be robust enough to reproduce the shear banding processes, particularly in sands, since it was originally developed to reproduce the hardening response of soils on the "wet" side of the critical state line, and not the dilative response on the "dry" side where this model poorly replicates the softening behavior necessary to trigger strain localization. To model the strain localization process more accurately, we use an alternative critical state formulation that contains an additional constitutive variable, namely, the state parameter ψ [37–39]. This parameter determines whether the state point lies below or above the critical state line, as well as enables a complete "detachment" of the yield surface from this line. By "detachment" we mean that the initial position of the critical state line and the state of stress alone do not determine the density of the material. Instead, one needs to specify the spatial variation of void ratio (or specific volume) *in addition* to the state parameters required by the classical Cam-Clay models. Through the state parameter ψ we can now prescribe quantitatively any measured specimen imperfection in the form of initial spatial density variation.

Specifically, we use classical plasticity theory along with a variant of "Nor-Sand" model proposed by Jefferies [38] to describe the constitutive law at the meso-scale level. The main difference between this and the classical Cam-Clay model lies in the description of the evolution of the plastic modulus. In classical Cam-Clay model the character of the plastic modulus depends on the sign of the plastic volumetric strain increment (determined from the flow rule), i.e., it is positive under compaction (hardening), negative under dilation (softening), and is zero at critical state (perfect plasticity). In sandy soils this may not be an accurate representation of hardening/softening responses since a dense sand could exhibit an initially contractive behavior, followed by a dilative behavior, when sheared. This important feature, called phase transformation in the literature [40,41], cannot be reproduced by classical Cam-Clay models. In the present formulation the growth or collapse of the yield surface is determined by the deviatoric component of the plastic strain increment and by the position of

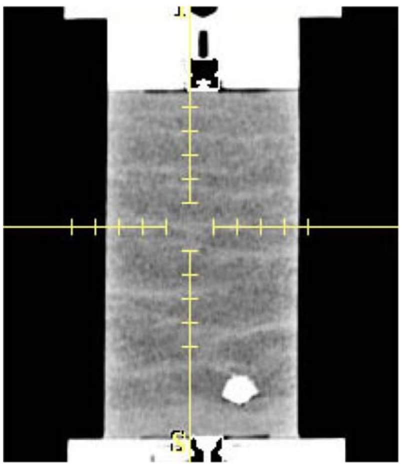

Fig. 1. Cross-section through a biaxial test specimen of silica sand analyzed by X-ray computed tomography; white spot is a piece of gravel.

the stress point relative to a so-called limit hardening dilatancy. Such description reproduces more accurately the softening response on the "dry" side of the critical state line.

The theoretical and computational aspects of this paper include the mathematical analyses of the thermodynamics of constitutive models characterized by elastoplastic coupling [42,43]. We also describe the numerical implementation of the finite deformation version of the model, the impact of B-bar integration near the critical state, and the localization of deformation on the "dry" side of the critical state line. We present two numerical examples demonstrating the localization of deformation in plane strain and full 3D loading conditions, highlighting in both cases the important role that the spatial density variation plays on the mechanical responses of dense granular materials.

Notations and symbols used in this paper are as follows: bold-faced letters denote tensors and vectors; the symbol '·' denotes an inner product of two vectors (e.g. $\boldsymbol{a}\cdot\boldsymbol{b} = a_i b_i$), or a single contraction of adjacent indices of two tensors (e.g. $\boldsymbol{c}\cdot\boldsymbol{d} = c_{ij}d_{jk}$); the symbol ':' denotes an inner product of two second-order tensors (e.g. $\boldsymbol{c}:\boldsymbol{d} = c_{ij}d_{ij}$), or a double contraction of adjacent indices of tensors of rank two and higher (e.g. $\boldsymbol{C} : \boldsymbol{\epsilon}^e = C_{ijkl}\epsilon^e_{kl}$); the symbol '⊗' denotes a juxtaposition, e.g., $(\boldsymbol{a}\otimes\boldsymbol{b})_{ij} = a_i b_j$. Finally, for any symmetric second-order tensors $\boldsymbol{\alpha}$ and $\boldsymbol{\beta}$, $(\boldsymbol{\alpha}\otimes\boldsymbol{\beta})_{ijkl} = \alpha_{ij}\beta_{kl}$, $(\boldsymbol{\alpha}\oplus\boldsymbol{\beta})_{ijkl} = \alpha_{jl}\beta_{ik}$, and $(\boldsymbol{\alpha}\ominus\boldsymbol{\beta})_{ijkl} = \alpha_{il}\beta_{jk}$.

2. Formulation of the infinitesimal model

We begin by presenting the general features of the meso-scale constitutive model in the infinitesimal regime. Extension of the features to the finite deformation regime is then presented in the next section.

2.1. Hyperelastic response

We consider a stored energy density function $\Psi^e(\boldsymbol{\epsilon}^e)$ in a granular assembly taken as a continuum; the macroscopic stress $\boldsymbol{\sigma}$ is given by

$$\boldsymbol{\sigma} = \frac{\partial \Psi^e}{\partial \boldsymbol{\epsilon}^e}, \tag{2.1}$$

where

$$\Psi^e = \widetilde{\Psi}^e(\epsilon^e_v) + \frac{3}{2}\mu^e \epsilon^{e2}_s, \tag{2.2}$$

and

$$\widetilde{\Psi}(\epsilon^e_v) = -p_0\tilde{\kappa}\exp\omega, \qquad \omega = -\frac{\epsilon^e_v - \epsilon^e_{v0}}{\tilde{\kappa}}, \qquad \mu^e = \mu_0 + \frac{\alpha_0}{\tilde{\kappa}}\widetilde{\Psi}(\epsilon^e_v). \tag{2.3}$$

The independent variables are the infinitesimal macroscopic volumetric and deviatoric strain invariants

$$\epsilon^e_v = \mathrm{tr}(\boldsymbol{\epsilon}^e), \qquad \epsilon^e_s = \sqrt{\frac{2}{3}}\|\boldsymbol{e}^e\|, \qquad \boldsymbol{e}^e = \boldsymbol{\epsilon}^e - \frac{1}{3}\epsilon^e_v\mathbf{1}, \tag{2.4}$$

where $\boldsymbol{\epsilon}^e$ is the elastic component of the infinitesimal macroscopic strain tensor. The material parameters required for definition are the reference strain ϵ^e_{v0} and reference pressure p_0 of the elastic compression curve, as well as the elastic compressibility index $\tilde{\kappa}$. The above model produces pressure-dependent elastic bulk and shear moduli, in accord with a well-known soil behavioral feature. Eq. (2.3) results in a constant elastic shear modulus $\mu^e = \mu_0$ when $\alpha_0 = 0$. This model is conservative in the sense that no energy is generated or lost in a closed elastic loading loop [44].

2.2. Yield surface, plastic potential function, and flow rule

We consider the first two stress invariants

$$p = \frac{1}{3}\mathrm{tr}\,\boldsymbol{\sigma}, \qquad q = \sqrt{\frac{3}{2}}\|\boldsymbol{s}\|, \quad \boldsymbol{s} = \boldsymbol{\sigma} - p\mathbf{1}, \tag{2.5}$$

where $p \leqslant 0$ in general. We define a yield function F of the form

$$F = q + \eta p, \tag{2.6}$$

where

$$\eta = \begin{cases} M[1+\ln(p_i/p)] & \text{if } N = 0, \\ (M/N)[1-(1-N)(p/p_i)^{N/(1-N)}] & \text{if } N > 0. \end{cases} \tag{2.7}$$

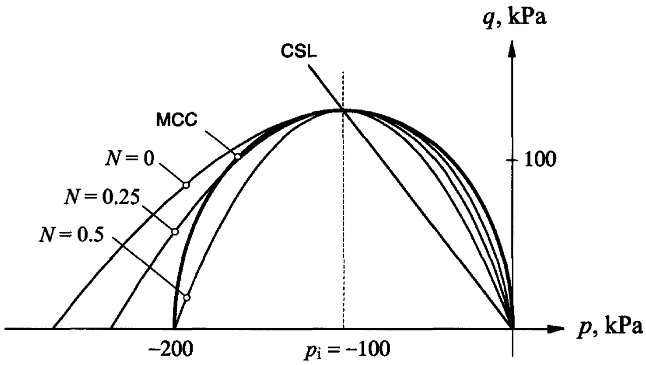

Fig. 2. Comparison of shapes of critical state yield surfaces.

Here, $p_i < 0$ is called the "image stress" representing the size of the yield surface, defined such that the stress ratio $\eta = -q/p = M$ when $p = p_i$. A closed-form expression for p_i is

$$\frac{p_i}{p} = \begin{cases} \exp(\eta/M - 1) & \text{if } N = 0, \\ [(1-N)/(1-\eta N/M)]^{(1-N)/N} & \text{if } N > 0. \end{cases} \tag{2.8}$$

The parameter $N \geqslant 0$ determines the curvature of the yield surface on the hydrostatic axis and typically has a value less than 0.4 for sands [38]; as N increases, the curvature increases. Fig. 2 shows yield surfaces for different values of N. For comparison, a plot of the conventional elliptical yield surface used in modified Cam-Clay plasticity theory is also shown [30].

Next we consider a plastic potential function of the form

$$Q = q + \bar{\eta} p, \tag{2.9}$$

where

$$\bar{\eta} = \begin{cases} M[1 + \ln(\bar{p}_i/p)] & \text{if } \overline{N} = 0, \\ (M/\overline{N})[1 - (1-\overline{N})(p/\bar{p}_i)^{\overline{N}/(1-\overline{N})}] & \text{if } \overline{N} > 0. \end{cases} \tag{2.10}$$

The plastic flow is associative if $\overline{N} = N$ and $\bar{p}_i = p_i$, and non-associative otherwise. For the latter case, we assume that $\overline{N} \leqslant N$ resulting in a plastic potential function that is 'flatter' than the yield surface (if $\overline{N} < N$), as shown in Fig. 3. This effectively yields a smaller dilatancy angle than is predicted by the assumption of associative normality, similar in idea to the thermodynamic restriction that the dilatancy angle must be at most equal to the friction angle in Mohr–Coulomb or Drucker–Prager materials, see [45,46] for further elaboration.

The variable $\bar{p}_i$ is a free parameter that determines the final size of the plastic potential function. If we set $Q = 0$ whenever the stress point (p, q) lies on the yield surface, then $\bar{p}_i$ can be determined as

$$\frac{\bar{p}_i}{p} = \begin{cases} \exp(\bar{\eta}/M - 1) & \text{if } \overline{N} = 0, \\ [(1-\overline{N})/(1-\bar{\eta}\overline{N}/M)]^{(1-\overline{N})/\overline{N}} & \text{if } \overline{N} > 0. \end{cases} \tag{2.11}$$

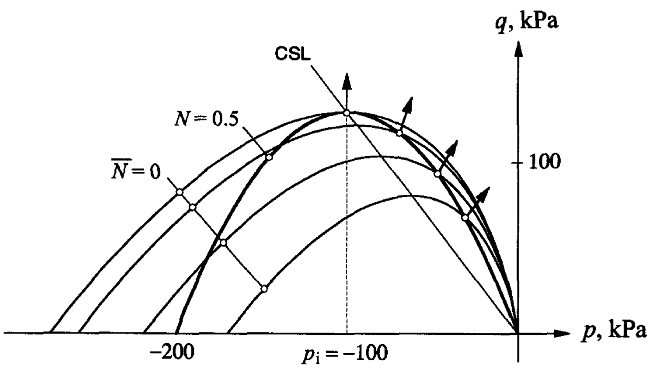

Fig. 3. Yield function and family of plastic potential surfaces.

The flow rule then writes

$$\dot{\boldsymbol{\epsilon}}^p = \dot{\lambda}\boldsymbol{q}, \qquad \boldsymbol{q} := \frac{\partial Q}{\partial \boldsymbol{\sigma}}, \tag{2.12}$$

where $\dot{\lambda} \geqslant 0$ is a non-negative plastic multiplier, and

$$\boldsymbol{q} = \frac{\partial q}{\partial \boldsymbol{\sigma}} + \bar{\eta}\frac{\partial p}{\partial \boldsymbol{\sigma}} + p\frac{\partial \bar{\eta}}{\partial \boldsymbol{\sigma}} = -\frac{1}{3}\left(\frac{M-\bar{\eta}}{1-\overline{N}}\right)\mathbf{1} + \sqrt{\frac{3}{2}}\frac{\boldsymbol{s}}{\|\boldsymbol{s}\|}, \quad \overline{N} \geqslant 0. \tag{2.13}$$

In this case, the variable $\bar{p}_i$ does not have to enter into the formulation since $\bar{\eta}$ can be determined directly from the relation $\bar{\eta} = \eta$.

The first two invariants of $\dot{\boldsymbol{\epsilon}}^p$ are

$$\dot{\epsilon}_v^p = \operatorname{tr}\dot{\boldsymbol{\epsilon}}^p = -\dot{\lambda}\left(\frac{M-\eta}{1-\overline{N}}\right), \qquad \dot{\epsilon}_s^p = \sqrt{\frac{2}{3}}\|\dot{\boldsymbol{e}}^p\| = \dot{\lambda}, \quad \dot{\boldsymbol{e}}^p = \dot{\boldsymbol{\epsilon}}^p - \frac{1}{3}\dot{\epsilon}_v^p\mathbf{1}, \tag{2.14}$$

where $\overline{N} \geqslant 0$. Note that $\dot{\epsilon}_v^p > 0$ (dilation) whenever $\eta > M$, and $\dot{\epsilon}_v^p < 0$ (compaction) whenever $\eta < M$. Plastic flow is purely isochoric when $\dot{\epsilon}_v^p = 0$, which occurs when $\eta = M$. Furthermore, note that

$$\boldsymbol{f} := \frac{\partial F}{\partial \boldsymbol{\sigma}} = \frac{\partial q}{\partial \boldsymbol{\sigma}} + \eta\frac{\partial p}{\partial \boldsymbol{\sigma}} + p\frac{\partial \eta}{\partial \boldsymbol{\sigma}} = -\frac{1}{3}\left(\frac{M-\eta}{1-N}\right)\mathbf{1} + \sqrt{\frac{3}{2}}\frac{\boldsymbol{s}}{\|\boldsymbol{s}\|}, \quad N \geqslant 0. \tag{2.15}$$

Since $\operatorname{tr}\boldsymbol{f} = 0$ whenever $\eta = M$, then plastic flow is always associative at this stress state regardless of the values of $\overline{N}$ and N. Non-associative plastic flow is possible only in the volumetric sense for this two-invariant model.

For perfect plasticity the reduced dissipation inequality requires the stresses to perform non-negative plastic incremental work [47], i.e.,

$$\mathscr{D}^p = \boldsymbol{\sigma} : \dot{\boldsymbol{\epsilon}}^p = \dot{\lambda}\boldsymbol{\sigma} : \boldsymbol{q} \geqslant 0. \tag{2.16}$$

Using the stress tensor decomposition $\boldsymbol{\sigma} = \boldsymbol{s} + p\mathbf{1}$ and substituting relation (2.13) into (2.16), we obtain

$$\mathscr{D}^p = -\dot{\lambda}\left(\eta + \frac{M-\bar{\eta}}{1-\overline{N}}\right)p \geqslant 0 \Rightarrow \eta + \frac{M-\bar{\eta}}{1-\overline{N}} \geqslant 0 \tag{2.17}$$

since $p \leqslant 0$. Now, if the stress point is on the yield surface then (2.7) determines the stress ratio η, and (2.17) thus becomes

$$-\frac{M\overline{N}}{N}\left[1-(1-N)\left(\frac{p}{p_i}\right)^{N/(1-N)}\right] + M \geqslant 0. \tag{2.18}$$

However, $M > 0$ since this is a physical parameter, and so we get

$$\overline{N} \leqslant N\left[1-(1-N)\left(\frac{p}{p_i}\right)^{N/(1-N)}\right]^{-1}. \tag{2.19}$$

The expression inside the pair of brackets is equal to unity at the stress space origin when $p = 0$, reduces to N at the image stress point when $\eta = M$ and $p = p_i$, and is zero on the hydrostatic axis when $\eta = 0$ and $p = p_i/(1-N)^{(1-N)/N}$. The corresponding inverses are equal to unity, $1/N > 1$, and positive infinity, respectively. Hence, for (2.19) to remain true at all times, we must have

$$\overline{N} \leqslant N, \tag{2.20}$$

as postulated earlier.

2.3. State parameter and plastic dilatancy

In classical Cam-Clay models the image stress p_i coincides with a point on the critical state line (CSL), a locus of points characterized by isochoric plastic flow in the space defined by the stress invariants p and q and by the specific volume v. The CSL is given by the pair of equations

$$q_c = -Mp_c, \qquad v_c = v_{c0} - \tilde{\lambda}\ln(-p_c), \tag{2.21}$$

where subscript "c" denotes that the point (v_c, p_c, q_c) is on the CSL. The parameters are the compressibility index $\tilde{\lambda}$ and the reference specific volume v_{c0}. Thus, any given point on the yield surface has an associated specific volume, and isochoric plastic flow can only take place on the CSL.

To apply the model to sands, which exhibit different types of volumetric yielding depending on initial density, the yield surface is detached from the critical state line along the v-axis. Thus, the state point (v, p, q) may now lie either above or below the critical specific volume v_c at the same stress p depending on whether the sand is looser or denser than critical. Following the notations of [38], a state parameter ψ is introduced to denote the relative distance along the v-axis of the current state point to a point v_c on the CSL at the same p,

$$\psi = v - v_c. \tag{2.22}$$

Further, a state parameter ψ_i is introduced denoting the distance of the same current state point to $v_{c,i}$ on the CSL at $p = p_i$,

$$\psi_i = v - v_{c,i}, \qquad v_{c,i} = v_{c0} - \tilde{\lambda} \ln(-p_i), \tag{2.23}$$

where $v_{c,i}$ is the value of v_c at the stress p_i, and v_{c0} is the reference value of v_c when $p_i = 1$, see (2.21). The relation between ψ and ψ_i is (see Fig. 4)

$$\psi_i = \psi + \tilde{\lambda} \ln\left(\frac{p_i}{p}\right). \tag{2.24}$$

Hence, ψ is negative below the CSL and positive above it. An upshot of disconnecting the yield surface from the CSL is that it is no longer possible to locate a state point on the yield surface by prescribing p and q alone; one also needs to specify the state parameter ψ to completely describe the state of a point. Furthermore, isochoric plastic flow does not anymore occur only on the CSL but could also take place at the image stress point. Finally, the parameter ψ_i dictates the amount of plastic dilatancy in the case of dense sands.

Formally, plastic dilatancy is defined by the expression

$$D := \dot{\epsilon}_v^p / \dot{\epsilon}_s^p = \frac{\eta - M}{1 - \overline{N}}. \tag{2.25}$$

This definition is valid for all possible values of η, even for $\eta = 0$ where Q is not a smooth function. However, experimental evidence on a variety of sands suggests that there exists a maximum possible plastic dilatancy, D^*, which limits a plastic hardening response. The value of D^* depends on the state parameter ψ_i, increasing in value as the state point lies farther and farther away from the CSL on the dense side. An empirical correlation has been established experimentally in [38] between the plastic dilatancy D^* and the state parameter ψ_i, and takes the form

$$D^* = \alpha \psi_i, \tag{2.26}$$

where $\alpha \approx -3.5$ typically for most sands. The corresponding value of stress ratio at this limit hardening dilatancy is

$$\eta^* = M + D^*(1 - \overline{N}) = M + \alpha\psi_i(1 - \overline{N}) = M + \bar{\alpha}\psi_i(1 - N), \tag{2.27}$$

and the corresponding size of the yield surface is

$$\frac{p_i^*}{p} = \begin{cases} \exp(\bar{\alpha}\psi_i/M) & \text{if } \overline{N} = N = 0, \\ (1 - \bar{\alpha}\psi_i N/M)^{(N-1)/N} & \text{if } 0 \leqslant \overline{N} \leqslant N \neq 0, \end{cases} \tag{2.28}$$

where

$$\bar{\alpha}\beta = \alpha, \qquad \beta = \frac{1 - N}{1 - \overline{N}}. \tag{2.29}$$

In the above expression we have introduced a non-associativity parameter $\beta \leqslant 1$, where $\beta = 1$ in the associative case.

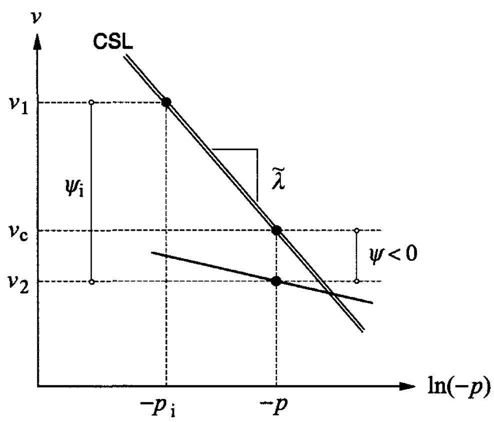

Fig. 4. Geometric representation of state parameter ψ.

2.4. Consistency condition and hardening law

For elastoplastic response the standard consistency condition on the yield function F reads

$$\dot{F} = \boldsymbol{f} : \dot{\boldsymbol{\sigma}} - H\dot{\lambda} = 0, \quad \dot{\lambda} > 0, \tag{2.30}$$

where H is the plastic modulus given by the equation

$$H = -\frac{1}{\dot{\lambda}}\frac{\partial F}{\partial p_i}\dot{p}_i = -\frac{1}{\dot{\lambda}}\left(\frac{p}{p_i}\right)^{1/(1-N)} M\dot{p}_i. \tag{2.31}$$

Since $p/p_i > 0$, the sign of the plastic modulus depends on the sign of $\dot{p}_i : H > 0$ if $\dot{p}_i < 0$ (hardening), $H < 0$ if $\dot{p}_i > 0$ (softening), and $H = 0$ if $\dot{p}_i = 0$ (perfect plasticity).

In classical Cam-Clay theory the sign of H depends on the sign of $\dot{\epsilon}_v^p$, i.e., H is positive for compaction and negative for expansion. However, as noted above, this simple criterion does not adequately capture the hardening/softening responses of sands, which are shown to be dependent on the limit hardening plastic dilatancy D^*, i.e., H is positive if $D < D^*$ and negative if $D > D^*$. Thus, any postulated hardening law must satisfy the obvious relationship

$$\operatorname{sgn} H = \operatorname{sgn}(-\dot{p}_i) = \operatorname{sgn}(D^* - D) = \operatorname{sgn}(\eta^* - \eta) = \operatorname{sgn}(p_i - p_i^*), \tag{2.32}$$

where 'sgn' is the sign operator. Furthermore, in terms of the cumulative plastic shear strain

$$\epsilon_s^p = \int_t \dot{\epsilon}_s^p \, \mathrm{d}t, \tag{2.33}$$

we require that

$$\lim_{\epsilon_s^p \to \infty} H = \lim_{\epsilon_s^p \to \infty} (-\dot{p}_i) = \lim_{\epsilon_s^p \to \infty} (D^* - D) = \lim_{\epsilon_s^p \to \infty} (\eta^* - \eta) = \lim_{\epsilon_s^p \to \infty} (p_i - p_i^*) = 0. \tag{2.34}$$

Thus, any postulated hardening law must reflect a condition of perfect plasticity as the plastic shear strain becomes very large. Note that the above restriction is stronger, e.g., than the weaker condition $D^* - D = 0$, without the limit, which could occur even if the stress and image points do not coincide. The limiting condition $\epsilon_s^p \to \infty$ insures that the stress and image points approach the CSL, and that these two points coincide in the limit.

A general evolution for $-\dot{p}_i$ satisfying the requirements stated above may be given by an equation of the form

$$-\dot{p}_i = f(p_i - p_i^*)\dot{\epsilon}_s^p = f(p_i - p_i^*)\dot{\lambda}, \tag{2.35}$$

where f is a simple odd scalar function of its argument, i.e., $f(-x) = -f(x)$ and $\operatorname{sgn} f = \operatorname{sgn} x$. (Alternately, one can use either D or η in the argument for f.) In this case, the expression for the plastic modulus becomes

$$H = M\left(\frac{p}{p_i}\right)^{1/(1-N)} f(p_i - p_i^*). \tag{2.36}$$

Taking $f(x) = hx$, where h is a positive dimensionless constant, we arrive at a phenomenological expression of the form similar to that presented in [38],

$$f(p_i - p_i^*) = h(p_i - p_i^*). \tag{2.37}$$

This results in a plastic modulus given by the equation

$$H = Mh\left(\frac{p}{p_i}\right)^{1/(1-N)} (p_i - p_i^*). \tag{2.38}$$

To summarize, the transition point between hardening and softening responses is represented by the limit hardening dilatancy D^*, which approaches zero on the CSL.

2.5. Implications to entropy production

Consider the Helmholtz free energy density function $\Psi = \Psi(\boldsymbol{\epsilon}^e, \epsilon_s^p)$. For now, we avoid making the usual additive decomposition of the free energy into $\Psi = \Psi^e(\boldsymbol{\epsilon}^e) + \Psi^p(\epsilon_s^p)$; in fact, we shall demonstrate that such decomposition is not possible in the present model. Ignoring the non-mechanical powers, the local Clausius–Duhem inequality yields

$$\boldsymbol{\sigma} : \dot{\boldsymbol{\epsilon}} - \frac{\mathrm{d}\Psi}{\mathrm{d}t} \geqslant 0. \tag{2.39}$$

Applying the chain rule for $\mathrm{d}\Psi/\mathrm{d}t$ and invoking the standard Coleman relations results in the constitutive relation

$$\boldsymbol{\sigma} = \frac{\partial \Psi(\boldsymbol{\epsilon}^e, \epsilon_s^p)}{\partial \boldsymbol{\epsilon}^e}, \tag{2.40}$$

plus the reduced dissipation inequality

$$\boldsymbol{\sigma} : \dot{\boldsymbol{\epsilon}}^p - p_i \dot{\epsilon}_s^p \geqslant 0, \qquad p_i = \frac{\partial \Psi(\boldsymbol{\epsilon}^e, \epsilon_s^p)}{\partial \epsilon_s^p}. \tag{2.41}$$

Here, we have chosen p_i to be the stress-like plastic internal variable conjugate to ϵ_s^p. With an appropriate set of material parameters we have ensured before that $\boldsymbol{\sigma} : \dot{\boldsymbol{\epsilon}}^p \geqslant 0$ (see Section 2.2). Since $\dot{\epsilon}_s^p = \dot{\lambda} \geqslant 0$ and $p_i < 0$, the reduced dissipation inequality as written above holds provided that

$$\frac{\partial \Psi(\boldsymbol{\epsilon}^e, \epsilon_s^p)}{\partial \epsilon_s^p} \leqslant 0. \tag{2.42}$$

Now, consider the evolution for p_i as postulated in (2.35). Integrating in time yields

$$\frac{\partial \Psi(\boldsymbol{\epsilon}^e, \epsilon_s^p)}{\partial \epsilon_s^p} \equiv p_i = p_{i0} - \int_{\epsilon_{s0}^p}^{\epsilon_s^p} f(p_i - p_i^*)\, \mathrm{d}\epsilon_s^p, \tag{2.43}$$

where p_{i0} is the reference value of p_i when $\epsilon_s^p = \epsilon_{s0}^p$. Recalling that f is a simple odd function, the right-hand side of the above equation is negative provided that $\operatorname{sgn}(p_i - p_i^*) = \operatorname{sgn} H =$ positive. This implies that the reduced dissipation inequality is identically satisfied in the hardening regime.

Integrating once more gives a more definitive form of the Helmholtz free energy,

$$\Psi(\boldsymbol{\epsilon}^e, \epsilon_s^p) = \int_{\epsilon_{s0}^p}^{\epsilon_s^p} p_{i0} \mathrm{d}\epsilon_s^p - \int_{\epsilon_{s0}^p}^{\epsilon_s^p} \int_{\epsilon_{s0}^p}^{\epsilon_s^p} f(p_i - p_i^*)\, \mathrm{d}\epsilon_s^p\, \mathrm{d}\epsilon_s^p + \Psi^e(\boldsymbol{\epsilon}^e) + \Psi_0, \tag{2.44}$$

where $\Psi^e(\boldsymbol{\epsilon}^e)$ is the usual elastic stored energy function. The first two integrals represent the plastic component of the free energy,

$$\Psi^p = \Psi^p(\boldsymbol{\epsilon}^e, \epsilon_s^p) = \int_{\epsilon_{s0}^p}^{\epsilon_s^p} p_{i0}\, \mathrm{d}\epsilon_s^p - \int_{\epsilon_{s0}^p}^{\epsilon_s^p} \int_{\epsilon_{s0}^p}^{\epsilon_s^p} f(p_i - p_i^*)\, \mathrm{d}\epsilon_s^p\, \mathrm{d}\epsilon_s^p. \tag{2.45}$$

Note in this case that Ψ^p depends not only on ϵ_s^p but also on $\boldsymbol{\epsilon}^e$ through the variable p_i^*. The Cauchy stress tensor then becomes

$$\boldsymbol{\sigma} = \frac{\partial \Psi^e(\boldsymbol{\epsilon}^e)}{\partial \boldsymbol{\epsilon}^e} + \underbrace{\int_{\epsilon_{s0}^p}^{\epsilon_s^p} \int_{\epsilon_{s0}^p}^{\epsilon_s^p} f'(p_i - p_i^*) \frac{\partial p_i^*}{\partial \boldsymbol{\epsilon}^e} \mathrm{d}\epsilon_s^p\, \mathrm{d}\epsilon_s^p}_{\mathrm{O}(\Delta\epsilon_s^{p2})}, \tag{2.46}$$

where $\Delta\epsilon_s^p = \epsilon_s^p - \epsilon_{s0}^p$, and

$$\frac{\partial p_i^*}{\partial \boldsymbol{\epsilon}^e} = (1 - N) \frac{\bar{\alpha} p_i^*/M}{1 - \bar{\alpha}\psi_i N/M} \frac{\partial \psi_i}{\partial \boldsymbol{\epsilon}^e} + \frac{p_i^*}{p} \frac{\partial p}{\partial \boldsymbol{\epsilon}^e}, \quad N \geqslant 0. \tag{2.47}$$

Strictly, then, the Cauchy stress tensor depends not only on $\boldsymbol{\epsilon}^e$ but also on ϵ_s^p. Attempts have been made in the past to capture this dependence of $\boldsymbol{\sigma}$ on ϵ_s^p; for example, a nonlinear elasticity model in which the elastic shear modulus varies with a stress-like plastic internal variable similar to p_i has been proposed in [43,48]. However, these developments have not gained much acceptance in the literature due, primarily, to the lack of experimental data and to the difficulty with obtaining such test data.

It must be noted that the observed dependence of Ψ^p on the elastic strain $\boldsymbol{\epsilon}^e$ occurs only prior to reaching the critical state where $\Delta\epsilon_s^p$ remains "relatively small", and thus, the second-order term in (2.46) may be ignored (such as done in Section 2.1). Most of the intense shearing (i.e., large $\Delta\epsilon_s^p$) in fact occurs at the critical state where $f(p_i - p_i^*) = 0$, at which condition the additive decomposition of the free energy into $\Psi^e(\boldsymbol{\epsilon}^e)$ and $\Psi^p(\epsilon_s^p)$ holds, see (2.44).

2.6. Numerical implementation

Even though the plastic internal variable p_i depends on the state parameter ψ_i, and that this variable is deeply embedded in the plastic modulus H, the model is still amenable to fully implicit numerical integration. Box 1 summarizes the relevant rate equations used in the constitutive theory. Box 2 summarizes the algorithmic counterpart utilizing the classical return mapping scheme. For improved efficiency, the return mapping algorithm in Box 2 is performed in the strain invariant space, Box 1. Summary of rate equations for plasticity model for sands, infinitesimal deformation version

1. Strain rates: $\dot{\boldsymbol{\epsilon}} = \dot{\boldsymbol{\epsilon}}^e + \dot{\boldsymbol{\epsilon}}^p$.
2. Hyperelastic rate equations: $\dot{\boldsymbol{\sigma}} = \boldsymbol{c}^e : \dot{\boldsymbol{\epsilon}}^e$; $\boldsymbol{c}^e = \partial^2 \Psi^e / \partial \boldsymbol{\epsilon}^e \partial \boldsymbol{\epsilon}^e$.
3. Flow rule: $\dot{\boldsymbol{\epsilon}}^p = \dot{\lambda} \boldsymbol{q}$.
4. State parameter: $\dot{\psi}_i = \dot{v} + \tilde{\lambda} \dot{p}_i / p_i$ from (2.23).
5. Hardening law: $-\dot{p}_i = f(p_i - p_i^*)\dot{\lambda}$ from (2.35).
6. Consistency condition: $\boldsymbol{f} : \dot{\boldsymbol{\sigma}} - H\dot{\lambda} = 0$.
7. Kuhn–Tucker conditions: $\dot{\lambda} \geqslant 0$, $F \leqslant 0$, $\dot{\lambda} F = 0$.

as demonstrated below, leading to a system of nonlinear equations with three unknowns. As usual, it is assumed that $\Delta\boldsymbol{\epsilon}$ is given, which implies that both the elastic trial strain $\boldsymbol{\epsilon}^{\mathrm{e\,tr}}$ and the total strain $\boldsymbol{\epsilon}$ are known. Note that v_0 is the initial value of the specific volume at the beginning of the calculations when $\boldsymbol{\epsilon} = \boldsymbol{0}$, and should not be confused with v_{c0}. As usual, the main goal is to find the final stresses $\boldsymbol{\sigma}$ and the discrete plastic multiplier $\Delta\lambda$ for a given strain increment $\Delta\boldsymbol{\epsilon}$.

Following [34,46], consider the following local residual equations generated by the applied strain increment $\Delta\boldsymbol{\epsilon}$

$$\boldsymbol{r} = \boldsymbol{r}(\boldsymbol{x}) = \left\{ \begin{array}{c} \epsilon_v^e - \epsilon_v^{\mathrm{e\,tr}} + \Delta\lambda\beta\partial_p F \\ \epsilon_s^e - \epsilon_s^{\mathrm{e\,tr}} + \Delta\lambda\partial_q F \\ F \end{array} \right\}; \qquad \boldsymbol{x} = \left\{ \begin{array}{c} \epsilon_v^e \\ \epsilon_s^e \\ \Delta\lambda \end{array} \right\}, \tag{2.48}$$

where β is the non-associativity parameter defined in (2.29). The goal is to dissipate the residual vector $\boldsymbol{r}$ by finding the solution vector $\boldsymbol{x}^*$ using a local Newton iteration.

In developing the local Jacobian matrix $\boldsymbol{r}'(\boldsymbol{x})$ used for Newton iteration, it is convenient to define the following mapping induced by the numerical algorithm

$$\boldsymbol{y} = \left\{ \begin{array}{c} p \\ q \\ p_i \end{array} \right\} = \left\{ \begin{array}{c} p(\epsilon_v^e, \epsilon_s^e) \\ q(\epsilon_v^e, \epsilon_s^e) \\ p_i(\epsilon_v^e, \epsilon_s^e, \Delta\lambda) \end{array} \right\} \Rightarrow \boldsymbol{y} = \boldsymbol{y}(\boldsymbol{x}). \tag{2.49}$$

The tangent $\boldsymbol{y}'(\boldsymbol{x}) = \boldsymbol{D}$ defines the slope, given by

$$\boldsymbol{D} = \begin{bmatrix} D_{11} & D_{12} & D_{13} \\ D_{21} & D_{22} & D_{23} \\ D_{31} & D_{32} & D_{33} \end{bmatrix} = \begin{bmatrix} \partial_{\epsilon_v^e} p & \partial_{\epsilon_s^e} p & 0 \\ \partial_{\epsilon_v^e} q & \partial_{\epsilon_s^e} q & 0 \\ \partial_{\epsilon_v^e} p_i & \partial_{\epsilon_s^e} p_i & \partial_{\Delta\lambda} p_i \end{bmatrix}. \tag{2.50}$$

Box 2. Return mapping algorithm for plasticity model for sands, infinitesimal deformation version

1. Elastic strain predictor: $\boldsymbol{\epsilon}^{\mathrm{e\,tr}} = \boldsymbol{\epsilon}_n^e + \Delta\boldsymbol{\epsilon}$.
2. Elastic stress predictor: $\boldsymbol{\sigma}^{\mathrm{tr}} = \partial\Psi^e / \partial\boldsymbol{\epsilon}^{\mathrm{e\,tr}}$; $p_i^{\mathrm{tr}} = p_{i,n}$.
3. Check if yielding: $F(\boldsymbol{\sigma}^{\mathrm{tr}}, p_i^{\mathrm{tr}}) \geqslant 0$?
   No, set $\boldsymbol{\epsilon}^e = \boldsymbol{\epsilon}^{\mathrm{e\,tr}}$; $\boldsymbol{\sigma} = \boldsymbol{\sigma}^{\mathrm{tr}}$; $p_i = p_i^{\mathrm{tr}}$ and exit.
4. Yes, initialize $\Delta\lambda = 0$ and iterate for $\Delta\lambda$ (steps 5–7).
5. Plastic corrector: $\boldsymbol{\epsilon}^e = \boldsymbol{\epsilon}^{\mathrm{e\,tr}} - \Delta\lambda\boldsymbol{q}$, $\boldsymbol{\sigma} = \partial\Psi^e / \partial\boldsymbol{\epsilon}^e$.
6. Update plastic internal variable p_i:
   (a) Cumulative strain: $\boldsymbol{\epsilon} = \boldsymbol{\epsilon}_n + \Delta\boldsymbol{\epsilon}$.
   (b) Specific volume: $v = v_0(1 + \mathrm{tr}\boldsymbol{\epsilon})$.
   (c) Initialize $p_i = p_{i,n}$ and iterate for p_i (steps 6d–f).
      (d) State parameter: $\psi_i = v - v_{c0} + \tilde{\lambda}\ln(-p_i)$.
      (e) Limit hardening plastic variable:

$$p_i^* = p \times \begin{cases} \exp(\bar{\alpha}\psi_i / M) & \text{if } \overline{N} = N = 0; \\ (1 - \bar{\alpha}\psi_i N / M)^{(N-1)/N} & \text{if } 0 \leqslant \overline{N} \leqslant N \neq 0. \end{cases}$$

      (f) Plastic internal variable: $p_i = p_{i,n} - f(p_i - p_i^*)\Delta\lambda$.
7. Discrete consistency condition: $F(p, q, p_i) = 0$.

The hyperelastic equations take the following form independent of the discrete plastic multiplier $\Delta\lambda$ (and hence, $D_{13} = D_{23} = 0$)

$$p = p_0 \exp\omega\left[1 + \frac{3\alpha_0}{2\tilde{\kappa}}\epsilon_s^{e2}\right], \qquad q = 3(\mu_0 - \alpha_0 p_0 \exp\omega)\epsilon_s^e. \tag{2.51}$$

Thus,

$$\begin{aligned} D_{11} &= -\tfrac{p_0}{\tilde{\kappa}}\exp\omega\left[1 + \tfrac{3\alpha_0}{2\tilde{\kappa}}\epsilon_s^{e2}\right],\\ D_{22} &= 3\mu_0 - 3\alpha_0 p_0 \exp\omega,\\ D_{12} &= D_{21} = \tfrac{3p_0\alpha_0\epsilon_s^e}{\tilde{\kappa}}\exp\omega. \end{aligned} \tag{2.52}$$

We recall that $D_{21} = D_{12}$ from the postulated existence of an elastic stored energy function Ψ^e.

The plastic internal variable p_i is deeply embedded in the evolution equations and is best calculated iteratively, as shown in Box 2. First, from Step no. 6(f), we construct a scalar residual equation

$$r(p_i) = p_i - p_{i,n} + f(p_i - p_i^*)\Delta\lambda, \tag{2.53}$$

where p_i^* is calculated in succession from Step no. 6(e,d) of Box 2 using the current estimate for p_i. Using a sub-local Newton iteration, we determine the root that dissipates this residual iteratively. The sub-local scalar tangent operator takes the simple form

$$r'(p_i) = 1 + f'(p_i - p_i^*)\Delta\lambda\left[1 - \frac{\tilde{\lambda}\bar{\alpha}(1-N)}{M - \bar{\alpha}\psi_i N}\left(\frac{p_i^*}{p_i}\right)\right], \quad N \geqslant 0. \tag{2.54}$$

Having determined the converged value of p_i, we can then calculate the corresponding values of ψ_i and p_i^* and proceed with the following differentiation.

From Box 2, Step no. 6(f), we obtain the variation

$$\frac{\partial p_i}{\partial \epsilon_v^e} = -f'(p_i - p_i^*)\Delta\lambda\left(\frac{\partial p_i}{\partial \epsilon_v^e} - \frac{\partial p_i^*}{\partial \epsilon_v^e}\right). \tag{2.55}$$

From Step no. 6(e), we get

$$\frac{\partial p_i^*}{\partial \epsilon_v^e} = \left(\bar{\alpha} p_i^* \frac{1-N}{M - \bar{\alpha}\psi_i N}\right)\frac{\partial \psi_i}{\partial \epsilon_v^e} + \frac{p_i^*}{p}D_{11}, \quad N \geqslant 0. \tag{2.56}$$

From Step no. 6(d), we obtain

$$\frac{\partial \psi_i}{\partial \epsilon_v^e} = \frac{\tilde{\lambda}}{p_i}\frac{\partial p_i}{\partial \epsilon_v^e}. \tag{2.57}$$

Combining these last three equations gives

$$\begin{aligned} D_{31} &= \frac{\partial p_i}{\partial \epsilon_v^e} = c^{-1} f'(p_i - p_i^*)\Delta\lambda\left(\frac{p_i^*}{p}\right)D_{11};\\ c &= 1 + f'(p_i - p_i^*)\Delta\lambda\left[1 - \frac{\tilde{\lambda}\bar{\alpha}(1-N)}{M - \bar{\alpha}\psi_i N}\left(\frac{p_i^*}{p_i}\right)\right]. \end{aligned} \tag{2.58}$$

Note that c is the converged value of $r'(p_i)$ when $r = 0$, cf. (2.54). Following a similar procedure, we obtain

$$D_{32} = \frac{\partial p_i}{\partial \epsilon_s^e} = c^{-1} f'(p_i - p_i^*)\Delta\lambda\left(\frac{p_i^*}{p}\right)D_{12}. \tag{2.59}$$

Again, using the same implicit differentiation, we get

$$D_{33} = \frac{\partial p_i}{\partial \Delta\lambda} = -c^{-1} f(p_i - p_i^*). \tag{2.60}$$

For the hardening law adopted in [38], $f'(p_i - p_i^*)$ reduces to the constant h.

It is also convenient to define the following vector operator

$$\boldsymbol{H} = [H_1 \quad H_2 \quad H_3] = \left[\partial_{pp}^2 \quad \partial_{pq}^2 \quad \partial_{pp_i}^2\right]F. \tag{2.61}$$

For the yield function at hand, the elements of $\boldsymbol{H}$ are as follows. First, we obtain the first derivatives

$$\frac{\partial F}{\partial p} = \begin{cases} M\ln(p_i/p); & \text{if } N = 0, \\ (M/N)[1-(p/p_i)^{N/(1-N)}]; & \text{if } N > 0, \end{cases}$$
$$\frac{\partial F}{\partial q} = 1, \quad \frac{\partial F}{\partial p_i} = M\left(\frac{p}{p_i}\right)^{1/(1-N)}, \quad N \geqslant 0. \tag{2.62}$$

Then, for $N \geqslant 0$, we have

$$H_1 = -\frac{1}{1-N}\frac{M}{p}\left(\frac{p}{p_i}\right)^{N/(1-N)}, \quad H_2 = 0, \quad H_3 = \frac{1}{1-N}\frac{M}{p}\left(\frac{p}{p_i}\right)^{1/(1-N)}. \tag{2.63}$$

Finally, from the product formula induced by the chain rule, we define the vector operator $\boldsymbol{G}$,

$$\boldsymbol{G} = \boldsymbol{HD} = [\,G_1 \quad G_2 \quad G_3\,]. \tag{2.64}$$

The algorithmic local tangent operator for Newton iteration is then given by

$$\boldsymbol{r}'(\boldsymbol{x}) = \begin{bmatrix} 1+\Delta\lambda\beta G_1 & \Delta\lambda\beta G_2 & \beta(\partial_p F + \Delta\lambda G_3) \\ 0 & 1 & \partial_q F \\ (D_{11}\partial_p + D_{21}\partial_q + D_{31}\partial_{p_i})F & (D_{12}\partial_p + D_{22}\partial_q + D_{32}\partial_{p_i})F & D_{33}\partial_{p_i}F \end{bmatrix}. \tag{2.65}$$

Remark. The numerical algorithm described above entails two levels of nested Newton iterations to determine the local unknowns. An alternative approach would be to consider p_i as a fourth local unknown, along with ϵ_v^e, ϵ_s^e and $\Delta\lambda$, and solve them all iteratively in one single Newton loop. We have found that either approach works well for the problem at hand, and that either one demonstrates about the same computational efficiency.

2.7. Algorithmic tangent operator

The algorithmic tangent operator $\boldsymbol{c} = \partial\boldsymbol{\sigma}/\partial\boldsymbol{\epsilon}^{\mathrm{e\,tr}} \equiv \partial\boldsymbol{\sigma}/\partial\boldsymbol{\epsilon}$ is used for the global Newton iteration of the finite element problem. It has been shown in [49,50] that it can also be used in lieu of the theoretically correct elastoplastic constitutive operator $\boldsymbol{c}^{\mathrm{ep}}$ for detecting the onset of material instability, provided the step size is 'small'. To derive the algorithmic tangent operator, consider the following expression for the Cauchy stress tensor

$$\boldsymbol{\sigma} = p\mathbf{1} + \sqrt{\frac{2}{3}}q\hat{\mathbf{n}}, \tag{2.66}$$

where $\hat{\boldsymbol{n}} = \boldsymbol{s}/\|\boldsymbol{s}\| = \boldsymbol{e}^e/\|\boldsymbol{e}^e\| = \boldsymbol{e}^{\mathrm{e\,tr}}/\|\boldsymbol{e}^{\mathrm{e\,tr}}\|$ from the co-axiality of the principal directions. The chain rule then yields (see [34])

$$\boldsymbol{c} = \frac{\partial\boldsymbol{\sigma}}{\partial\boldsymbol{\epsilon}} = \mathbf{1}\otimes\left(D_{11}\frac{\partial\epsilon_v^e}{\partial\boldsymbol{\epsilon}} + D_{12}\frac{\partial\epsilon_s^e}{\partial\boldsymbol{\epsilon}}\right) + \sqrt{\frac{2}{3}}\hat{\boldsymbol{n}}\otimes\left(D_{21}\frac{\partial\epsilon_v^e}{\partial\boldsymbol{\epsilon}} + D_{22}\frac{\partial\epsilon_s^e}{\partial\boldsymbol{\epsilon}}\right) + \frac{2q}{3\epsilon_s^{\mathrm{e\,tr}}}\left(\boldsymbol{I} - \frac{1}{3}\mathbf{1}\otimes\mathbf{1} - \hat{\boldsymbol{n}}\otimes\hat{\boldsymbol{n}}\right), \tag{2.67}$$

where $\boldsymbol{I}$ is the fourth-rank identity tensor with components $I_{ijkl} = (\delta_{ik}\delta_{jl} + \delta_{il}\delta_{jk})/2$. Our goal is to obtain closed-form expressions for the derivatives $\partial\epsilon_v^e/\partial\boldsymbol{\epsilon}$ and $\partial\epsilon_s^e/\partial\boldsymbol{\epsilon}$.

Using the same strain invariant formulation of the previous section, we now write the same local residual vector as $\boldsymbol{r} = \boldsymbol{r}(\epsilon_v^{\mathrm{e\,tr}}, \epsilon_s^{\mathrm{e\,tr}}, \boldsymbol{x})$, where $\boldsymbol{x}$ is the vector of local unknowns. We recall that the trial elastic strains were held fixed at the local level; however, at the global level they themselves are now the iterates. Consequently, at the converged state where $\boldsymbol{r} = \mathbf{0}$, we now write the strain derivatives of the residual vector as

$$\frac{\partial\boldsymbol{r}}{\partial\boldsymbol{\epsilon}} = \left.\frac{\partial\boldsymbol{r}}{\partial\boldsymbol{\epsilon}}\right|_x + \left(\left.\frac{\partial\boldsymbol{r}}{\partial\boldsymbol{x}}\right|_{\epsilon_v^{\mathrm{e\,tr}},\epsilon_s^{\mathrm{e\,tr}}}\right)\cdot\frac{\partial\boldsymbol{x}}{\partial\boldsymbol{\epsilon}} = \mathbf{0}, \tag{2.68}$$

which gives

$$\boldsymbol{a}\cdot\frac{\partial\boldsymbol{x}}{\partial\boldsymbol{\epsilon}} = -\left.\frac{\partial\boldsymbol{r}}{\partial\boldsymbol{\epsilon}}\right|_x \Rightarrow \frac{\partial\boldsymbol{x}}{\partial\boldsymbol{\epsilon}} = -\boldsymbol{b}\cdot\left.\frac{\partial\boldsymbol{r}}{\partial\boldsymbol{\epsilon}}\right|_x. \tag{2.69}$$

We recognize $\boldsymbol{a}$ as the same 3×3 tangent matrix $\boldsymbol{r}'(\boldsymbol{x})$ in (2.65) evaluated *at the locally converged state*, and $\boldsymbol{b} = \boldsymbol{a}^{-1}$. In component form, we have

$$\left\{\begin{matrix} \partial\epsilon_v^e/\partial\boldsymbol{\epsilon} \\ \partial\epsilon_s^e/\partial\boldsymbol{\epsilon} \\ \partial\Delta\lambda/\partial\boldsymbol{\epsilon} \end{matrix}\right\} = \begin{bmatrix} b_{11} & b_{12} & b_{13} \\ b_{21} & b_{22} & b_{23} \\ b_{31} & b_{32} & b_{33} \end{bmatrix} \left\{\begin{matrix} (1-\Delta\lambda\beta\theta H_3)\mathbf{1} \\ \sqrt{2/3}\hat{\boldsymbol{n}} \\ -\theta\partial_{p_i}F\mathbf{1} \end{matrix}\right\}, \tag{2.70}$$

in which $\partial p_i/\partial\boldsymbol{\epsilon} = \theta\mathbf{1}$, and

$$\theta = c^{-1}\Delta\lambda f'(p_i - p_i^*)v_0 p_i^* \frac{\bar{\alpha}(1-N)}{M - \bar{\alpha}\psi_i N} \tag{2.71}$$

is the linearization of the term associated with the state parameter ψ_i. This facilitates the solution of the desired strain derivatives,

$$\frac{\partial\epsilon_v^e}{\partial\boldsymbol{\epsilon}} = \tilde{b}_{11}\mathbf{1} + \sqrt{\frac{2}{3}}b_{12}\hat{\boldsymbol{n}}, \quad \frac{\partial\epsilon_s^e}{\partial\boldsymbol{\epsilon}} = \tilde{b}_{21}\mathbf{1} + \sqrt{\frac{2}{3}}b_{22}\hat{\boldsymbol{n}}, \tag{2.72}$$

where

$$\begin{aligned} \tilde{b}_{11} &= (1-\Delta\lambda\beta\theta H_3)b_{11} - (\theta\partial_{p_i}F)b_{13}, \\ \tilde{b}_{21} &= (1-\Delta\lambda\beta\theta H_3)b_{21} - (\theta\partial_{p_i}F)b_{23}. \end{aligned} \tag{2.73}$$

Defining the matrix product

$$\begin{bmatrix} \overline{D}_{11} & \overline{D}_{12} \\ \overline{D}_{21} & \overline{D}_{22} \end{bmatrix} = \begin{bmatrix} D_{11} & D_{12} \\ D_{21} & D_{22} \end{bmatrix} \begin{bmatrix} \tilde{b}_{11} & b_{12} \\ \tilde{b}_{21} & b_{22} \end{bmatrix}, \tag{2.74}$$

the consistent tangent operator then becomes

$$\boldsymbol{c} = \left(\overline{D}_{11} - \frac{2q}{9\epsilon_s^{\mathrm{e\,tr}}}\right)\mathbf{1}\otimes\mathbf{1} + \sqrt{\frac{2}{3}}\left(\overline{D}_{12}\mathbf{1}\otimes\hat{\boldsymbol{n}} + \overline{D}_{21}\hat{\boldsymbol{n}}\otimes\mathbf{1}\right) + \frac{2q}{3\epsilon_s^{\mathrm{e\,tr}}}(\boldsymbol{I} - \hat{\boldsymbol{n}}\otimes\hat{\boldsymbol{n}}) + \frac{2}{3}\overline{D}_{22}\hat{\boldsymbol{n}}\otimes\hat{\boldsymbol{n}}. \tag{2.75}$$

In the elastic regime the submatrix $[b_{ij}]$ becomes an identity matrix, and hence $\overline{D}_{ij} = D_{ij}$ for $i,j = 1,2$. In this case, $\boldsymbol{c}$ reduces to the hyperelastic tangent operator $\boldsymbol{c}^e$.

Remark. As shown in Fig. 3, the proposed yield and plastic potential functions create corners on the compaction side of the hydrostatic axis. While the model is primarily developed to accurately capture dilative plastic flow, and therefore is not expected to perform well in stress states dominated by hydrostatic compaction, numerical problems could still arise in general boundary-value problem simulations when the stress ratio η as defined by (2.7) goes to zero or even becomes negative. In order to avoid a negative η, we introduce a 'cap' on the plastic potential function such that

$$Q = \begin{cases} q + \bar{\eta}p & \text{if } \bar{\eta} = \eta \geqslant \chi M, \\ -p & \text{if } \bar{\eta} = \eta < \chi M, \end{cases} \tag{2.76}$$

where χ is a user-specified parameter controlling the position of the plastic potential function cap, e.g., $\chi = 0.10$. For the case where $\bar{\eta} < \chi M$, the local residual vector simplifies to

$$\boldsymbol{r}(\boldsymbol{x}) = \left\{\begin{matrix} \epsilon_v^e - \epsilon_v^{\mathrm{e\,tr}} - \Delta\lambda \\ \epsilon_s^e - \epsilon_s^{\mathrm{e\,tr}} \\ F \end{matrix}\right\}. \tag{2.77}$$

The local tangent operator is given by

$$\boldsymbol{r}'(\boldsymbol{x}) = \begin{bmatrix} 1 & 0 & -1 \\ 0 & 1 & 0 \\ (D_{11}\partial_p + D_{21}\partial_q)F & (D_{12}\partial_p + D_{22}\partial_q)F & 0 \end{bmatrix}. \tag{2.78}$$

Finally, the strain derivative of $\boldsymbol{r}$ holding $\boldsymbol{x}$ fixed reduces to

$$\left.\frac{\partial\boldsymbol{r}}{\partial\boldsymbol{\epsilon}}\right|_x = \left\{\begin{matrix} \mathbf{1} \\ \sqrt{2/3}\hat{\boldsymbol{n}} \\ \mathbf{0} \end{matrix}\right\}. \tag{2.79}$$

Of course, one can also insert a smooth cap near the nose of the plastic potential function as an alternative to the planar cap.

3. Finite deformation plasticity; localization of deformation

In the preceding section we have reformulated an infinitesimal rigid-plastic constitutive model for sands to accommodate non-associated plasticity and hyperelasticity. In this section we further generalize the model to accommodate finite deformation plasticity. The final model is then used to capture deformation and failure initiation in dense sands, focusing on the effects of uneven void distribution on the local and global responses.

3.1. Entropy inequality

Consider the multiplicative decomposition of deformation gradient for a local material point X [51–53]

$$\boldsymbol{F}(X,t) = \boldsymbol{F}^e(X,t) \cdot \boldsymbol{F}^p(X,t). \tag{3.1}$$

In the following we shall use as a measure of elastic deformation the contravariant tensor field $\boldsymbol{b}^e$ reckoned with respect to the current placement, called the left Cauchy–Green deformation tensor,

$$\boldsymbol{b}^e = \boldsymbol{F}^e \cdot \boldsymbol{F}^{\mathrm{et}}. \tag{3.2}$$

Assume then that the free energy is given by

$$\Psi = \Psi(X, \boldsymbol{b}^e, \varepsilon_s^p). \tag{3.3}$$

As in the infinitesimal model, we investigate conditions under which we could isolate an elastic stored energy function from the above free energy function.

For the purely mechanical theory the local dissipation function takes the form

$$\mathscr{D} = \boldsymbol{\tau} : \boldsymbol{d} - \frac{\mathrm{d}\Psi(X, \boldsymbol{b}^e, \varepsilon_s^p)}{\mathrm{d}t} \geqslant 0, \tag{3.4}$$

where $\boldsymbol{\tau} = J\boldsymbol{\sigma}$ is the symmetric Kirchhoff stress tensor, $J = \det(\boldsymbol{F})$, $\boldsymbol{d} = \mathrm{sym}(\boldsymbol{l})$ is the rate of deformation tensor, and $\boldsymbol{l}$ is the spatial velocity gradient. Using the chain rule and invoking the standard Coleman relations yields the constitutive equation [54]

$$\boldsymbol{\tau} = 2\frac{\partial \Psi(X, \boldsymbol{b}^e, \varepsilon_s^p)}{\partial \boldsymbol{b}^e} \cdot \boldsymbol{b}^e, \tag{3.5}$$

along with the reduced dissipation inequality

$$\mathscr{D} = \boldsymbol{\tau} : \boldsymbol{d}^p - \pi_i \dot{\varepsilon}_s^p \geqslant 0, \tag{3.6}$$

where $\boldsymbol{d}^p$ is the plastic component of the rate of deformation,

$$\boldsymbol{d}^p = \mathrm{sym}(\boldsymbol{l}^p), \quad \boldsymbol{l}^p := \boldsymbol{F}^e \cdot \boldsymbol{L}^p \cdot \boldsymbol{F}^{e-1}, \quad \boldsymbol{L}^p := \dot{\boldsymbol{F}}^p \cdot \boldsymbol{F}^{p-1}, \tag{3.7}$$

and

$$\pi_i = \frac{\partial \Psi(X, \boldsymbol{b}^e, \varepsilon_s^p)}{\partial \varepsilon_s^p} \tag{3.8}$$

is a stress-like plastic internal variable equivalent to p_{i} of the infinitesimal theory.

We assume that π_i evolves in the same way as p_i, i.e.,

$$-\dot{\pi}_i = \phi(\pi_i - \pi_i^*)\dot{\varepsilon}_s^p, \tag{3.9}$$

where π_i^* depends not only on π_i but also on $\boldsymbol{b}^e$. Integrating (3.9) gives

$$\pi_i = \pi_{i0} - \int_{\varepsilon_{s0}^p}^{\varepsilon_s^p} \phi(\pi_i - \pi_i^*)\,\mathrm{d}\varepsilon_s^p. \tag{3.10}$$

Integrating once more, we get

$$\Psi(X, \boldsymbol{b}^e, \varepsilon_s^p) = \int_{\varepsilon_{s0}^p}^{\varepsilon_s^p} \pi_{i0}\,\mathrm{d}\varepsilon_s^p - \int_{\varepsilon_{s0}^p}^{\varepsilon_s^p}\int_{\varepsilon_{s0}^p}^{\varepsilon_s^p} \phi(\pi_i - \pi_i^*)\,\mathrm{d}\varepsilon_s^p\,\mathrm{d}\varepsilon_s^p + \Psi^e(X, \boldsymbol{b}^e) + \Psi_0, \tag{3.11}$$

where $\Psi^e(X, \boldsymbol{b}^e)$ is the elastic stored energy function. Finally, using the constitutive Eq. (3.5) once again, we get

$$\boldsymbol{\tau} = 2\left[\frac{\partial \Psi^e(X, \boldsymbol{b}^e)}{\partial \boldsymbol{b}^e} + \underbrace{\int_{\varepsilon_{s0}^p}^{\varepsilon_s^p}\int_{\varepsilon_{s0}^p}^{\varepsilon_s^p} \phi'(\pi_i - \pi_i^*)\frac{\partial \pi_i^*}{\partial \boldsymbol{b}^e}\,\mathrm{d}\varepsilon_s^p\,\mathrm{d}\varepsilon_s^p}_{\mathrm{O}(\Delta\varepsilon_s^{p2})}\right] \cdot \boldsymbol{b}^e. \tag{3.12}$$

The second-order terms in (3.12) can be ignored at the initial stage of loading when $\Delta\varepsilon_s^p$ is small, thus leaving the Kirchhoff stress varying with the elastic stored energy function alone. When $\Delta\varepsilon_s^p$ is large, $\phi(\pi_i - \pi_i^*)$ vanishes at critical state, and so the elastic and plastic parts of the free energy uncouple. In both cases the stresses can be expressed in terms of the elastic stored energy function alone, i.e.,

$$\boldsymbol{\tau} = 2\frac{\partial \Psi^e(X, \boldsymbol{b}^e)}{\partial \boldsymbol{b}^e} \cdot \boldsymbol{b}^e. \tag{3.13}$$

Once again, the perfectly plastic behavior at critical state is a key feature of the model that allows for the uncoupling of the free energy.

3.2. Finite deformation plasticity model

Consider the stress invariants

$$p = \frac{1}{3}\operatorname{tr}\boldsymbol{\tau}, \qquad q = \sqrt{\frac{3}{2}}\|\boldsymbol{\xi}\|, \qquad \boldsymbol{\xi} = \boldsymbol{\tau} - p\mathbf{1}. \tag{3.14}$$

Then, as in the infinitesimal theory the yield function can be defined as

$$F = q + \eta p \leqslant 0, \tag{3.15}$$

where

$$\eta = \begin{cases} M[1 + \ln(\pi_i/p)] & \text{if } N = 0, \\ (M/N)[1 - (1-N)(p/\pi_i)^{N/(1-N)}] & \text{if } N > 0. \end{cases} \tag{3.16}$$

The material parameters M and N are similar in meaning to those of the infinitesimal theory, although their values should now be calibrated in the finite deformation regime. The flow rule may be written as before,

$$\boldsymbol{d}^p = \dot{\lambda}\boldsymbol{q}, \qquad \boldsymbol{q} = \frac{\beta}{3}\frac{\partial F}{\partial p}\mathbf{1} + \sqrt{\frac{3}{2}}\frac{\partial F}{\partial q}\hat{\boldsymbol{n}}, \qquad \hat{\boldsymbol{n}} = \boldsymbol{\xi}/\|\boldsymbol{\xi}\|, \tag{3.17}$$

where $\beta \leqslant 1$ is the non-associativity parameter. We postulate a similar hardening law in Kirchhoff stress space given by (3.9), with

$$\operatorname{sgn}[\phi(\pi_i - \pi_i^*)] = \operatorname{sgn} H \tag{3.18}$$

to capture either a hardening or softening response depending on the position of the state point relative to the limit hardening dilatancy. Box 3 then summarizes the rate equations for the finite deformation plasticity model.

The model summarized in Box 3 has some noteworthy features. First, the formulation assumes that the plastic spin $\boldsymbol{\omega}^p$ is zero (see [55] for some discussions on the significance of the plastic spin). Second, the fourth-order spatial elastic tangent operator $\boldsymbol{\alpha}^e$ can be determined from the expression

$$\boldsymbol{\alpha}^e = \mathbf{c}^e + \boldsymbol{\tau} \oplus \mathbf{1} + \boldsymbol{\tau} \ominus \mathbf{1}, \tag{3.19}$$

where $(\boldsymbol{\tau} \oplus \mathbf{1})_{ijkl} = \tau_{jl}\delta_{ik}$, $(\boldsymbol{\tau} \ominus \mathbf{1})_{ijkl} = \tau_{il}\delta_{jk}$, and $\mathbf{c}^e$ is a spatial tangential elasticity tensor obtained from the push-forward of all the indices of the second tangential elasticity tensor defined in [53].

Box 3. Summary of rate equations for plasticity model for sands, finite deformation version

1. Velocity gradient: $\boldsymbol{l} = \boldsymbol{l}^e + \boldsymbol{l}^p$.
2. Hyperelastic rate equation: $\dot{\boldsymbol{\tau}} = \boldsymbol{\alpha}^e : \boldsymbol{l}^e$.
3. Flow rule: $\boldsymbol{d}^p = \operatorname{sym}(\boldsymbol{l}^p) = \dot{\lambda}\boldsymbol{q}, \quad \boldsymbol{\omega}^p = \operatorname{skw}(\boldsymbol{l}^p) = \mathbf{0}$.
4. State parameter: $\dot{\psi}_i = \dot{v} + \tilde{\lambda}\dot{\pi}_i/\pi_i$.
5. Hardening law: $-\dot{\pi}_i = \phi(\pi_i - \pi_i^*)\dot{\lambda}$.
6. Consistency condition: $\boldsymbol{f} : \dot{\boldsymbol{\tau}} - H\dot{\lambda} = 0, \quad \boldsymbol{f} = \partial F/\partial\boldsymbol{\tau}$.
7. Kuhn–Tucker conditions: $\dot{\lambda} \geqslant 0, \quad F \leqslant 0, \quad \dot{\lambda}F = 0$.

Finally, the specific volume varies according to the kinematical relation

$$v = Jv_0 \Rightarrow \dot{v} = \dot{J}v_0 = Jv_0\operatorname{tr}(\boldsymbol{l}) = v\operatorname{tr}(\boldsymbol{l}). \tag{3.20}$$

Thus, just as in the infinitesimal theory where the rate equations may be viewed as driven by the strain rate $\dot{\boldsymbol{\epsilon}}$, the rate equations shown in Box 3 may be viewed as driven by the spatial velocity gradient $\boldsymbol{l}$.

3.3. Numerical implementation

For the problem at hand we employ a standard elastic predictor-plastic corrector algorithm based on the product formula for $\boldsymbol{b}^e$, as summarized in Box 4. Let

$$\boldsymbol{b}^e_n = \boldsymbol{F}^e_n \cdot \boldsymbol{F}^{et}_n. \tag{3.21}$$

Suppressing plastic flow, the trial elastic predictor for $\boldsymbol{b}^e$ is

$$\boldsymbol{b}^{e\,\mathrm{tr}} \equiv \boldsymbol{b}^{e\,\mathrm{tr}}_{n+1} = \boldsymbol{f}_{n+1} \cdot \boldsymbol{b}^e_n \cdot \boldsymbol{f}^t_{n+1}, \quad \boldsymbol{f}_{n+1} = \frac{\partial \boldsymbol{x}_{n+1}}{\partial \boldsymbol{x}_n}. \tag{3.22}$$

The plastic corrector emanates from the exponential approximation

$$\boldsymbol{b}^e = \exp(-2\Delta\lambda \boldsymbol{q}) \cdot \boldsymbol{b}^{e\,\mathrm{tr}}, \quad \boldsymbol{q} \equiv \boldsymbol{q}_{n+1} = \frac{\partial Q}{\partial \boldsymbol{\tau}}. \tag{3.23}$$

From the co-axiality of plastic flow, the principal directions of $\boldsymbol{q}$ and $\boldsymbol{\tau}$ coincide.

Box 4. Return mapping algorithm for plasticity model for sands, finite deformation version

1. Elastic deformation predictor: $\boldsymbol{b}^{e\,\mathrm{tr}} = \boldsymbol{f}_{n+1} \cdot \boldsymbol{b}^e_n \cdot \boldsymbol{f}^t_{n+1}$.
2. Elastic stress predictor: $\boldsymbol{\tau}^{\mathrm{tr}} = 2(\partial \Psi^e / \partial \boldsymbol{b}^{e\,\mathrm{tr}}) \cdot \boldsymbol{b}^{e\,\mathrm{tr}}$; $\quad \pi_i^{\mathrm{tr}} = \pi_{i,n}$.
3. Check if yielding: $F(p^{\mathrm{tr}}, q^{\mathrm{tr}}, \pi_i^{\mathrm{tr}}) \geqslant 0$?
   No, set $\boldsymbol{b}^e = \boldsymbol{b}^{e\,\mathrm{tr}}$; $\quad \boldsymbol{\tau} = \boldsymbol{\tau}^{\mathrm{tr}}$; $\quad \pi_i = \pi_i^{\mathrm{tr}}$ and exit.
4. Yes, initialize $\Delta\lambda = 0$ and iterate for $\Delta\lambda$ (steps 5–8).
5. Spectral decomposition: $\boldsymbol{b}^{e\,\mathrm{tr}} = \sum_{A=1}^{3} (\lambda_A^{e\,\mathrm{tr}})^2 \boldsymbol{m}^{\mathrm{tr}(A)}$.
6. Plastic corrector in principal logarithmic stretches: $\varepsilon_A^e = \ln(\lambda_A^e)$, $\quad \varepsilon_A^{e\,\mathrm{tr}} = \ln(\lambda_A^{e\,\mathrm{tr}})$,
   $\varepsilon_A^e = \varepsilon_A^{e\,\mathrm{tr}} - \Delta\lambda q_A$, $\quad \tau_A = \partial \overline{\Psi}^e / \partial \varepsilon_A^e$, $\quad A = 1, 2, 3$.
7. Update plastic internal variable π_i:
   (a) Total deformation gradient: $\boldsymbol{F} = \boldsymbol{f}_{n+1} \cdot \boldsymbol{F}_n$.
   (b) Specific volume: $v = \det(\boldsymbol{F}) v_0 = J v_0$.
   (c) Initialize $\pi_i = \pi_{i,n}$ and iterate for π_i (Steps 7d–f).
      (d) State parameter: $\psi_i = v - v_{c0} + \tilde{\lambda} \ln(-\pi_i)$.
      (e) Limit hardening plastic variable:
$$\pi_i^* = p \times \begin{cases} \exp(\bar{\alpha}\psi_i / M) & \text{if } \overline{N} = N = 0; \\ (1 - \bar{\alpha}\psi_i N / M)^{(N-1)/N} & \text{if } 0 \leqslant \overline{N} \leqslant N \neq 0. \end{cases}$$
      (f) Plastic internal variable: $\pi_i = \pi_{i,n} - \phi(\pi_i - \pi_i^*)\Delta\lambda$.
8. Discrete consistency condition: $F(p, q, \pi_i) = 0$.
9. Spectral resolution: $\boldsymbol{b}^e = \sum_{A=1}^{3} (\lambda_A^e)^2 \boldsymbol{m}^{\mathrm{tr}(A)}$.

Next we obtain a spectral decomposition of $\boldsymbol{b}^e$,

$$\boldsymbol{b}^e = \sum_{A=1}^{3} (\lambda_A^e)^2 \boldsymbol{m}^{(A)}, \quad \boldsymbol{m}^{(A)} = \boldsymbol{n}^{(A)} \otimes \boldsymbol{n}^{(A)}, \tag{3.24}$$

where λ_A^e are the elastic principal stretches, $\boldsymbol{n}^{(A)}$ are the unit principal directions, and $\boldsymbol{m}^{(A)}$ are the spectral directions. The corresponding elastic logarithmic stretches are

$$\varepsilon_A^e = \ln(\lambda_A^e), \quad A = 1, 2, 3. \tag{3.25}$$

From material frame indifference $\Psi^e(X, \boldsymbol{b}^e)$ only varies with ε_A^e, and so we can write $\overline{\Psi}^e = \overline{\Psi}^e(X, \varepsilon_1^e, \varepsilon_2^e, \varepsilon_2^e)$, which gives

$$\frac{\partial \Psi^e}{\partial \boldsymbol{b}^e} = \frac{1}{2} \sum_{A=1}^{3} \frac{1}{(\lambda_A^e)^2} \frac{\partial \overline{\Psi}^e}{\partial \varepsilon_A^e} \boldsymbol{m}^{(A)}. \tag{3.26}$$

The elastic constitutive equation then writes

$$\boldsymbol{\tau} = 2\frac{\partial \Psi^e}{\partial \boldsymbol{b}^e}\cdot \boldsymbol{b}^e = \sum_{A=1}^{3}\tau_A \boldsymbol{m}^{(A)}, \qquad \tau_A = \frac{\partial \overline{\Psi}^e}{\partial \varepsilon_A^e}, \tag{3.27}$$

implying that the spectral directions of $\boldsymbol{\tau}$ and $\boldsymbol{b}^e$ also coincide. Thus, $\boldsymbol{b}^e$ and $\boldsymbol{q}$ are also co-axial, and for (3.23) to hold, $\boldsymbol{b}^e$ and $\boldsymbol{b}^{\mathrm{e\,tr}}$ must also be co-axial, i.e.,

$$\boldsymbol{m}^{(A)} = \boldsymbol{m}^{\mathrm{tr}(A)}. \tag{3.28}$$

This allows the plastic corrector phase to take place along the principal axes, as shown in Box 4.

Alternatively, we can utilize the algorithm developed for the infinitesimal theory by working on the invariant space of the logarithmic elastic stretch tensor. Let

$$\varepsilon_v^e = \varepsilon_1^e + \varepsilon_2^e + \varepsilon_3^e, \qquad \varepsilon_s^e = \frac{1}{3}\sqrt{2[(\varepsilon_1^e-\varepsilon_2^e)^2 + (\varepsilon_1^e-\varepsilon_3^e)^2 + (\varepsilon_2^e-\varepsilon_3^e)^2]} \tag{3.29}$$

denote the first two invariants of the logarithmic elastic stretch tensor (similar definitions may be made for $\varepsilon_v^{\mathrm{e\,tr}}$ and $\varepsilon_s^{\mathrm{e\,tr}}$), and

$$p = \frac{1}{3}(\tau_1+\tau_2+\tau_3), \qquad q = \sqrt{[(\tau_1-\tau_2)^2 + (\tau_1-\tau_3)^2 + (\tau_2-\tau_3)^2]/2} \tag{3.30}$$

denote the first two invariants of the Kirchhoff stress tensor. If we take the functional relationships $p = p(\varepsilon_v^e, \varepsilon_s^e)$, $q = q(\varepsilon_v^e, \varepsilon_s^e)$, and $\pi_i = \pi_i(\varepsilon_v^e, \varepsilon_s^e, \Delta\lambda)$ as before, using the same elastic stored energy function but now expressed in terms of the logarithmic principal elastic stretches, then the local residual vector writes

$$\boldsymbol{r} = \boldsymbol{r}(\boldsymbol{x}) = \begin{Bmatrix} \varepsilon_v^e - \varepsilon_v^{\mathrm{e\,tr}} + \Delta\lambda\beta\partial_p F \\ \varepsilon_s^e - \varepsilon_s^{\mathrm{e\,tr}} + \Delta\lambda\partial_q F \\ F \end{Bmatrix}, \qquad \boldsymbol{x} = \begin{Bmatrix} \varepsilon_v^e \\ \varepsilon_s^e \\ \Delta\lambda \end{Bmatrix}. \tag{3.31}$$

In this case, the local Jacobian $\boldsymbol{r}'(\boldsymbol{x})$ takes a form *identical* to that developed for the infinitesimal theory, see (2.65).

Comparing Boxes 2 and 4, we see that the algorithm for finite deformation plasticity differs from the infinitesimal version only through a few additional steps entailed for the spectral decomposition and resolution of the deformation and stress tensors. Construction of $\boldsymbol{b}^e$ from the spectral values requires two steps. The first involves resolution of the principal elastic logarithmic stretches from the first two invariants calculated from return mapping,

$$\varepsilon_A^e = \frac{1}{3}\varepsilon_v^e\delta_A + \sqrt{\frac{3}{2}}\varepsilon_s^e\hat{n}_A, \qquad \hat{n}_A = \sqrt{\frac{2}{3}}\frac{\varepsilon_A^{\mathrm{e\,tr}} - (\varepsilon_v^{\mathrm{e\,tr}}/3)\delta_A}{\varepsilon_s^{\mathrm{e\,tr}}}, \tag{3.32}$$

where $\delta_A = 1$ for $A = 1,2,3$. The above transformation entails scaling the deviatoric component of the predictor tensor by the factor $\varepsilon_s^e/\varepsilon_s^{\mathrm{e\,tr}}$ and adding the volumetric component. The second step involves a spectral resolution from the principal elastic logarithmic strains (cf. (3.24))

$$\boldsymbol{b}^e = \sum_{A=1}^{3}\exp(2\varepsilon_A^e)\boldsymbol{m}^{\mathrm{tr}(A)}. \tag{3.33}$$

The next section demonstrates that a closed-form consistent tangent operator is available for the above algorithm.

3.4. Algorithmic tangent operator

For simplicity, we restrict to a quasi-static problem whose weak form of the linear momentum balance over an initial volume $\mathscr{B}$ with surface $\partial\mathscr{B}$ reads

$$\int_{\mathscr{B}}(\mathrm{GRAD}\boldsymbol{\eta} : \boldsymbol{P} - \rho_0\boldsymbol{\eta}\cdot\boldsymbol{G})\,\mathrm{d}V - \int_{\partial\mathscr{B}^t}\boldsymbol{\eta}\cdot\boldsymbol{t}\,\mathrm{d}A = 0, \tag{3.34}$$

where $\rho_0\boldsymbol{G}$ is the reference body force vector, $\boldsymbol{t} = \boldsymbol{P}\cdot\boldsymbol{n}$ is the nominal traction vector on $\partial\mathscr{B}^t \subset \partial\mathscr{B}$, $\boldsymbol{n}$ is the unit vector on $\partial\mathscr{B}^t$, $\boldsymbol{\eta}$ is the weighting function,

$$\boldsymbol{P} = \boldsymbol{\tau}\cdot\boldsymbol{F}^{-t} \tag{3.35}$$

is the non-symmetric first Piola–Kirchhoff stress tensor, and GRAD is the gradient operator evaluated with respect to the reference configuration. We recall the internal virtual work

$$W^e_{\mathrm{INT}} = \int_{\mathscr{B}^e} \mathrm{GRAD}\boldsymbol{\eta} : \boldsymbol{P}\,\mathrm{d}V = \int_{\mathscr{B}^e} \mathrm{grad}\boldsymbol{\eta} : \boldsymbol{\tau}\,\mathrm{d}V \tag{3.36}$$

for any $\mathscr{B}^e \subset \mathscr{B}$, where grad is the gradient operator evaluated with respect to the current configuration. The first variation gives [56]

$$\delta W^e_{\mathrm{INT}} = \int_{\mathscr{B}^e} \mathrm{grad}\boldsymbol{\eta} : \mathbf{a} : \mathrm{grad}\delta\boldsymbol{u}\,\mathrm{d}V, \tag{3.37}$$

where $\boldsymbol{u}$ is the displacement field, and

$$\mathbf{a} = \boldsymbol{\alpha} - \boldsymbol{\tau} \ominus \mathbf{1}, \qquad \delta\boldsymbol{\tau} = \boldsymbol{\alpha} : \mathrm{grad}\delta\boldsymbol{u}. \tag{3.38}$$

Evaluation of $\mathbf{a}$ thus requires determination of the algorithmic tangent operator $\boldsymbol{\alpha}$.

We also recall the following spectral representation of the algorithmic tangent operator $\boldsymbol{\alpha}$ [56]

$$\boldsymbol{\alpha} = \sum_{A=1}^{3}\sum_{B=1}^{3} a_{AB}\boldsymbol{m}^{(A)} \otimes \boldsymbol{m}^{(B)} + \sum_{A=1}^{3}\sum_{B\neq A} \frac{\tau_B - \tau_A}{\lambda_B^{\mathrm{e\,tr}2} - \lambda_A^{\mathrm{e\,tr}2}}\left(\lambda_B^{\mathrm{e\,tr}2}\boldsymbol{m}^{(AB)} \otimes \boldsymbol{m}^{(AB)} + \lambda_A^{\mathrm{e\,tr}2}\boldsymbol{m}^{(AB)} \otimes \boldsymbol{m}^{(BA)}\right), \tag{3.39}$$

where $\boldsymbol{m}^{(AB)} = \boldsymbol{n}^{(A)} \otimes \boldsymbol{n}^{(B)}$, $A \neq B$. The coefficients a_{AB} are elements of the consistent tangent operator obtained from a return mapping in principal axes, and is formally defined as

$$a_{AB} = \frac{\partial \tau_A}{\partial \varepsilon_B^{\mathrm{e\,tr}}} \equiv \frac{\partial \tau_A}{\partial \varepsilon_B}, \quad A, B = 1, 2, 3. \tag{3.40}$$

The values of these coefficients are specific to the constitutive model in question, as well as dependent on the numerical integration algorithm utilized for the model. For the present critical state plasticity theory a_{AB} is evaluated as follows.

The expression for a principal Kirchhoff stress is

$$\tau_A = p\delta_A + \sqrt{\frac{2}{3}}q\hat{n}_A, \quad A = 1, 2, 3. \tag{3.41}$$

Differentiating with respect to a principal logarithmic strain gives

$$\begin{aligned} a_{AB} = \frac{\partial \tau_A}{\partial \varepsilon_B} &= \delta_A\left(D_{11}\frac{\partial \varepsilon_v^e}{\partial \varepsilon_B} + D_{12}\frac{\partial \varepsilon_s^e}{\partial \varepsilon_B}\right) + \sqrt{\frac{2}{3}}\hat{n}_A\left(D_{21}\frac{\partial \varepsilon_v^e}{\partial \varepsilon_B} + D_{22}\frac{\partial \varepsilon_s^e}{\partial \varepsilon_B}\right) \\ &\quad + \frac{2q}{3\varepsilon_s^{\mathrm{e\,tr}}}\left(\delta_{AB} - \frac{1}{3}\delta_A\delta_B - \hat{n}_A\hat{n}_B\right), \quad A, B = 1, 2, 3, \end{aligned} \tag{3.42}$$

where δ_{AB} is the Kronecker delta. The coefficients D_{11}, D_{22}, and D_{21} are identical in form to those shown in (2.52) except that the strain invariants now take on logarithmic definitions. As in the infinitesimal theory, we obtain the unknown strain derivatives above from the local residual vector, whose own derivatives write

$$\frac{\partial r_A}{\partial \varepsilon_B} = \left.\frac{\partial r_A}{\partial \varepsilon_B}\right|_x + \sum_{C=1}^{3} \underbrace{\left.\frac{\partial r_A}{\partial x_C}\right|_{\varepsilon_v^{\mathrm{e\,tr}},\varepsilon_s^{\mathrm{e\,tr}}}}_{\bar{a}_{AC}} \frac{\partial x_C}{\partial \varepsilon_B} = 0, \quad A, B = 1, 2, 3, \tag{3.43}$$

where the matrix $[\bar{a}_{AB}]$ corresponds to the same algorithmic local tangent operator given in (2.65). Letting $[b_{AB}]$ denote the inverse of $[\bar{a}_{AB}]$, we can then solve

$$\frac{\partial x_A}{\partial \varepsilon_B} = -\sum_{C=1}^{3} b_{AC}\left.\frac{\partial r_C}{\partial \varepsilon_B}\right|_x, \quad A, B = 1, 2, 3. \tag{3.44}$$

This latter equation provides the desired strain derivatives,

$$\begin{Bmatrix} \partial\varepsilon_v^e/\partial\varepsilon_A \\ \partial\varepsilon_s^e/\partial\varepsilon_A \\ \partial\Delta\lambda/\partial\varepsilon_A \end{Bmatrix} = \begin{bmatrix} b_{11} & b_{12} & b_{13} \\ b_{21} & b_{22} & b_{23} \\ b_{31} & b_{32} & b_{33} \end{bmatrix} \begin{Bmatrix} (1 - \Delta\lambda\beta\theta H_3)\delta_A \\ \sqrt{2/3}\hat{n}_A \\ -\theta\partial_{\pi_i}F\delta_A \end{Bmatrix}, \quad A = 1, 2, 3, \tag{3.45}$$

where

$$\begin{aligned} \theta &= c^{-1}\Delta\lambda\phi'(\pi_i - \pi_i^*)v\pi_i^*\frac{\bar{\alpha}(1-N)}{M - \bar{\alpha}\psi_i N}, \\ c &= 1 + \phi'(\pi_i - \pi_i^*)\Delta\lambda\left[1 - \frac{\tilde{\lambda}\bar{\alpha}(1-N)}{M - \bar{\alpha}\psi_i N}\left(\frac{\pi_i^*}{\pi_i}\right)\right]. \end{aligned} \tag{3.46}$$

Note that the finite deformation expression for θ utilizes the current value of the specific volume v whereas the infinitesimal version uses the initial value v_0 (cf. (2.71)). Inserting the expressions for $\partial\varepsilon_v^e/\partial\varepsilon_A$ and $\partial\varepsilon_s^e/\partial\varepsilon_A$ back in (3.42) yields the closed-form solution for a_{AB}, which takes an identical form to (2.75):

$$a_{AB} = \left(\overline{D}_{11} - \frac{2q}{9\varepsilon_s^{\mathrm{e\,tr}}}\right)\delta_A\delta_B + \sqrt{\frac{2}{3}}\left(\overline{D}_{12}\delta_A\hat{n}_B + \overline{D}_{21}\hat{n}_A\delta_B\right) + \frac{2q}{3\varepsilon_s^{\mathrm{e\,tr}}}(\delta_{AB} - \hat{n}_A\hat{n}_B) + \frac{2}{3}\overline{D}_{22}\hat{n}_A\hat{n}_B, \quad A,B = 1,2,3. \tag{3.47}$$

See (2.72)–(2.74) for specific expressions for the coefficients $\overline{D}_{ij}$.

3.5. Localization condition

Following [56,57], we summarize the following alternative (and equivalent) expressions for the localization condition into planar bands. We denote the continuum elastoplastic counterpart of the algorithmic tensor $\boldsymbol{\alpha}$ by

$$\boldsymbol{\alpha}^{\mathrm{ep}} = \sum_{A=1}^{3}\sum_{B=1}^{3} a_{AB}^{\mathrm{ep}}\boldsymbol{m}^{(A)}\otimes\boldsymbol{m}^{(B)} + \sum_{A=1}^{3}\sum_{B\neq A}\frac{\tau_B-\tau_A}{\lambda_B^{\mathrm{e}2}-\lambda_A^{\mathrm{e}2}}\left(\lambda_B^{\mathrm{e}2}\boldsymbol{m}^{(AB)}\otimes\boldsymbol{m}^{(AB)} + \lambda_A^{\mathrm{e}2}\boldsymbol{m}^{(AB)}\otimes\boldsymbol{m}^{(BA)}\right), \tag{3.48}$$

where a_{AB}^{ep} is the continuum elastoplastic tangent stiffness matrix in principal axes. (Note, this formula appears in [46,49,50] with a factor "1/2" before the spin-term summations, a typographical error.) Then,

$$\mathbf{a}^{\mathrm{ep}} = \boldsymbol{\alpha}^{\mathrm{ep}} - \boldsymbol{\tau}\ominus\mathbf{1} \tag{3.49}$$

defines the continuum counterpart of the fourth-order tensor $\mathbf{a}$ in (3.38).

Alternatively, we denote the constitutive elastoplastic material tensor $\mathbf{c}^{\mathrm{ep}}$ by the expression [54]

$$\mathbf{c}^{\mathrm{ep}} = \sum_{A=1}^{3}\sum_{B=1}^{3} a_{AB}^{\mathrm{ep}}\boldsymbol{m}^{(A)}\otimes\boldsymbol{m}^{(B)} + \sum_{A=1}^{3}\tau_A\boldsymbol{\omega}^{(A)}, \tag{3.50}$$

in which

$$\begin{aligned}\boldsymbol{\omega}^{(A)} = 2[&\boldsymbol{I}_b - \boldsymbol{b}^e\otimes\boldsymbol{b}^e + I_3 b_A^{-1}(\mathbf{1}\otimes\mathbf{1} - \boldsymbol{I}) + b_A(\boldsymbol{b}^e\otimes\boldsymbol{m}^{(A)} + \boldsymbol{m}^{(A)}\otimes\boldsymbol{b}^e)\\ &- I_3 b_A^{-1}(\mathbf{1}\otimes\boldsymbol{m}^{(A)} + \boldsymbol{m}^{(A)}\otimes\mathbf{1}) + \psi\boldsymbol{m}^{(A)}\otimes\boldsymbol{m}^{(A)}]/D_A,\end{aligned} \tag{3.51}$$

where b_A is the Ath principal value of $\boldsymbol{b}^e$, I_1 and I_3 are the first and third invariants of $\boldsymbol{b}^e$,

$$\boldsymbol{I}_b = (\boldsymbol{b}^e\oplus\boldsymbol{b}^e + \boldsymbol{b}^e\ominus\boldsymbol{b}^e)/2, \qquad \psi = I_1 b_A + I_3 b_A^{-1} - 4b_A^2, \tag{3.52}$$

and

$$D_A := 2b_A^2 - I_1 b_A + I_3 b_A^{-1}. \tag{3.53}$$

Note that $\mathrm{c}_{ijkl}^{\mathrm{ep}} = 2F_{iA}F_{jB}F_{kC}F_{lD}\mathrm{C}_{ABCD}^{\mathrm{ep}}$ is the spatial push-forward of the first tangential elastoplastic tensor $\mathbf{C}^{\mathrm{ep}}$ [53]. Then,

$$\mathbf{a}^{\mathrm{ep}} = \mathbf{c}^{\mathrm{ep}} + \boldsymbol{\tau}\oplus\mathbf{1} \tag{3.54}$$

defines an alternative expression to (3.49).

Using $\mathbf{a}^{\mathrm{ep}}$ from either (3.49) or (3.54), we can evaluate the elements of the Eulerian elastoplastic acoustic tensor $\boldsymbol{a}$ as

$$a_{ij} = n_k \mathrm{a}_{ikjl}^{\mathrm{ep}} n_l, \tag{3.55}$$

where n_k and n_l are elements of the unit normal vector $\boldsymbol{n}$ to a potential deformation band reckoned with respect to the current configuration. Defining the localization function as

$$\mathscr{F} = \inf|_n(\det\boldsymbol{a}), \tag{3.56}$$

we can then infer the inception of a deformation band from the initial vanishing of $\mathscr{F}$. Though theoretically one needs to use the constitutive operators $\boldsymbol{\alpha}^{\mathrm{ep}}$ or $\mathbf{c}^{\mathrm{ep}}$ to obtain the acoustic tensor $\boldsymbol{a}$, the algorithmic tangent tensors are equally acceptable for bifurcation analyses for small step sizes [50].

4. Numerical simulations

We present two numerical examples demonstrating the meso-scale modeling technique. To highlight the triggering of strain localization via imposed material inhomogeneity, we only considered regular specimens (either rectangular or cubical) along with boundary conditions favoring the development of homogeneous deformation (a pin to arrest rigid body modes and vertical rollers at the top and bottom ends of the specimen). A common technique of perturbing the initial condition is to prescribe a weak element; however, this is unrealistic and arbitrary. In the following simulations we have perturbed the initial condition by prescribing a spatially varying specific volume (or void ratio) consisting of horizontal layers of relatively homogeneous density but with some variation in the vertical direction. This resulted in vein-like soil structures in the density field closely resembling that shown in the photograph of Fig. 1 and mimicked the placement of sand with a common laboratory technique called pluviation. The specific volume fields were assumed to range from 1.60 to 1.70, with a mean value of 1.63. These values were chosen such that all points remained on the dense side of the CSL ($\psi_i < 0$).

4.1. Plane strain simulation

As a first example we considered a finite element mesh 1 m wide and 2 m tall and consisting of 4096 constant strain triangular elements shown in Fig. 5. The mesh is completely symmetric to avoid any bias introduced by the triangles. The vertical sides were subjected to pressure loads (natural boundary condition), whereas the top end was compressed by moving roller supports (essential boundary condition). The load–time functions are shown in Fig. 6 with scaling factors $\gamma = 100$ kPa and $\beta = 0.40$ m for pressure load $G_1(t)$ and vertical compression $G_2(t)$, respectively. The material parameters are summarized in Tables 1 and 2 and roughly represent those of dense Erksak sand, see [38]. The preconsolidation stress was set to $p_c = -130$ kPa and the reference specific volume was assumed to have a value $v_{c0} = 1.915$ (uniform for all elements). The distribution of initial specific volume is shown in Fig. 7.

Fig. 8 shows contours of the determinant function and the logarithmic deviatoric strains at the onset of localization for the case of finite deformations, which occurred at a nominal axial strain of 12.26%. Localization for the infinitesimal model was slightly delayed at 12.34%. The figure shows a clear correlation between regions in the specimen where the determinant function vanished for the first time and where the deviatoric strains were most intense. Furthermore, the figure reveals an

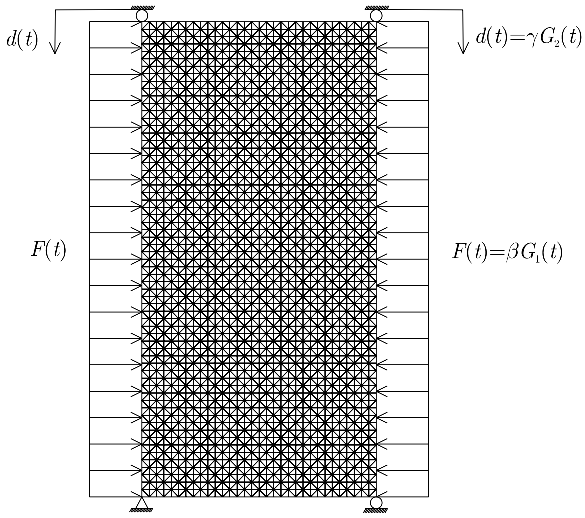

Fig. 5. Finite element mesh for plane strain compression problem.

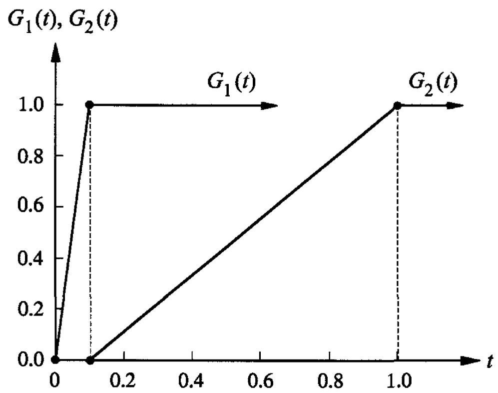

Fig. 6. Load–time functions.

Table 1
Summary of hyperelastic material parameters (see [44] for laboratory testing procedure)

Symbol	Value	Parameter
$\tilde{\kappa}$	0.03	Compressibility
α_0	0	Coupling coefficient
μ_0	2000 kPa	Shear modulus
p_0	−100 kPa	Reference pressure
ϵ^e_{v0}	0	Reference strain

Table 2
Summary of plastic material parameters (see [38] for laboratory testing procedure)

Symbol	Value	Parameter
$\tilde{\lambda}$	0.04	Compressibility
N	0.4	For yield function
$\overline{N}$	0.2	For plastic potential
h	280	Hardening coefficient

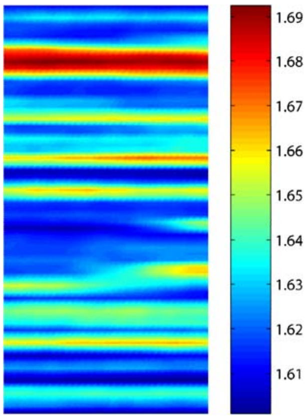

Fig. 7. Initial specific volume for plane strain compression problem.

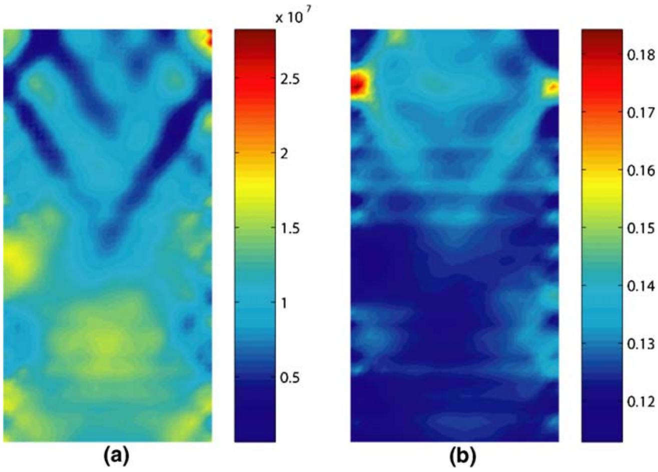

Fig. 8. Contours of: (a) determinant function; and (b) deviatoric invariant of logarithmic stretches at onset of strain localization.

X-pattern of shear band formation captured by both shear deformation and determinant function contours, reproducing those observed in laboratory experiments [3,5].

Fig. 9 displays contours of the plastic modulus and the logarithmic volumetric strains at the onset of localization. We recall that for this plasticity model the plastic modulus is a function of the state of stress, and in this figure low values of

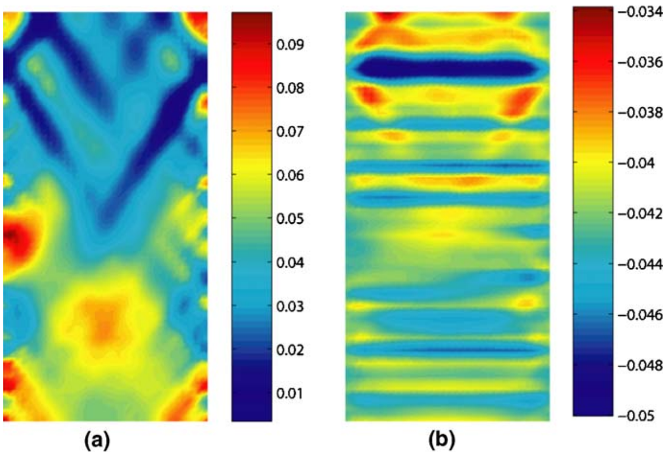

Fig. 9. Contours of: (a) plastic hardening modulus; and (b) volumetric invariant of logarithmic stretches at onset of strain localization.

hardening modulus correlate with areas of highly localized shear strains shown in Fig. 8. On the other hand, volumetric strains at localization appear to resemble the initial distribution of specific volume shown in Fig. 7. In fact the blue pocket of high compression extending horizontally at the top of the sample (Fig. 9b) is representative of that experienced by the red horizontal layer of relatively low density shown in Fig. 7. The calculated shear bands were predominantly dilative.

4.2. Three-dimensional simulation

For the 3D simulation we considered a cubical finite element mesh shown in Fig. 10. The mesh is 1 m wide by 1 m deep by 2 m tall and consists of 2000 eight-node brick elements. All four vertical faces of the mesh were subjected to pressure loads of 100 kPa (natural boundary condition). The top face at $z = 2$ m was compressed vertically by moving roller supports according to the same load–time function shown in Fig. 6 (essential boundary condition), effectively replicating a laboratory testing protocol for 'triaxial' compression on a specimen with a square cross-section. The initial distribution of specific volume is also shown in Fig. 10 and roughly mimicked the profile for plane strain shown in Fig. 7.

Figs. 11 and 12 compare the nominal axial stress and volume change behaviors, respectively, of specimens with and without imposed heterogeneities. The homogeneous specimen was created to have a uniform specific volume equal to the volume average of the specific volume for the equivalent heterogeneous specimen, or 1.63 in this case. We used both the standard numerical integration and B-bar method for the calculations [58–60], but there was not much difference in the predicted responses. However, softening within the range of deformation shown in these figures was detected by all solutions except by the homogeneous specimen simulation. Furthermore, an earlier overall dilation from an initially contractive behavior was detected by the heterogeneous specimen simulation (Fig. 12). This reversal in volume change behavior from contractive to dilative is usually termed 'phase transformation' in the geotechnical literature, a feature that is not replicated

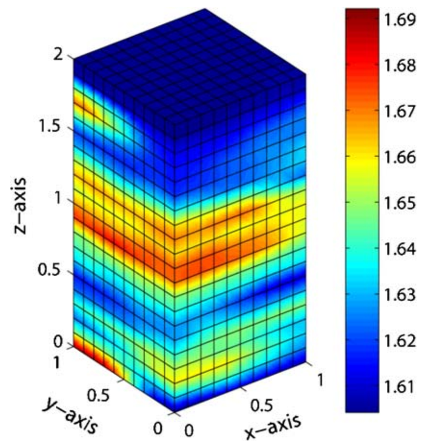

Fig. 10. Finite element mesh and initial specific volume for 3D compression problem.

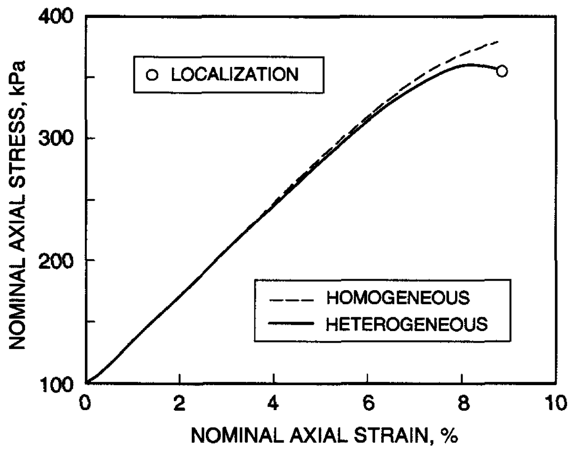

Fig. 11. Nominal axial stress–axial strain responses for 3D compression problem.

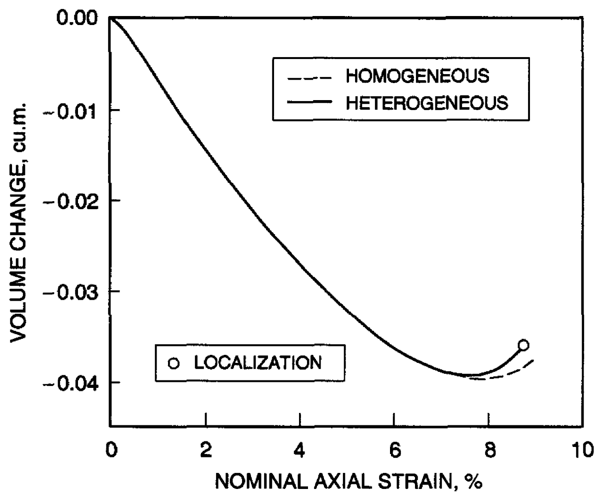

Fig. 12. Volume change-nominal axial strain responses for 3D compression problem.

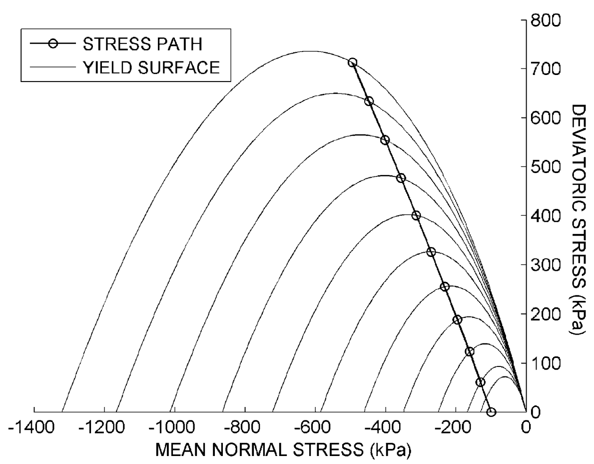

Fig. 13. Stress path for homogeneous specimen simulation with finite deformation.

by classical Cam-Clay models. Fig. 13 shows that this phase transition was captured by the constitutive model by first yielding on the compression side of the yield surface, and later by yielding on the dilation side.

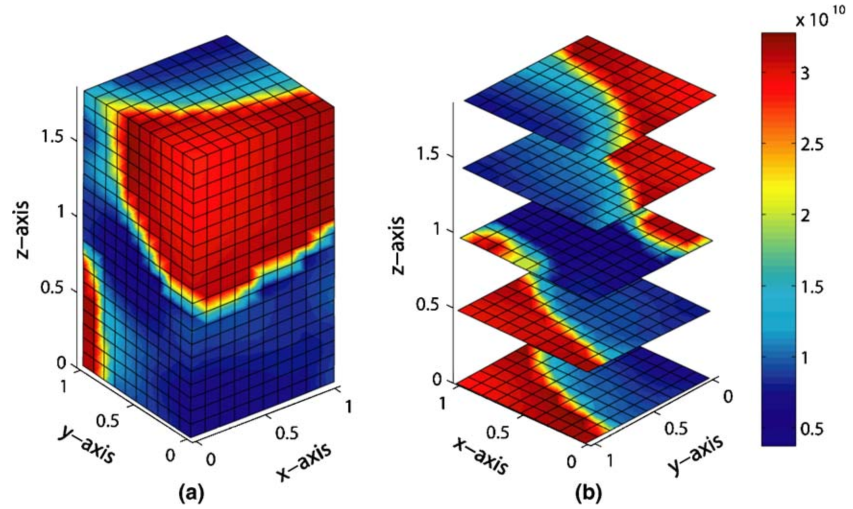

Fig. 14. Determinant function at onset of strain localization.

Fig. 14 shows contours of the determinant function $\mathscr{F}$ at a nominal axial strain of 8.78%, where the determinant vanished for the first time at a Gauss point located in the interior of the heterogeneous specimen. Unlike the plane strain solution, the potential shear band did not exhibit an X-pattern in this case. Instead, the solution predicted a well-defined band extending across the specimen. Note that the horizontal slices shown in Fig. 14b have been rotated by 90° on the horizontal plane relative to the orientation of the solid volume shown in Fig. 14a for optimal 3D visualization (red regions in Fig. 14a must be matched with red regions in Fig. 14b, etc.). As for the homogeneous specimen, the computation was carried out up to 15% nominal axial strain but the sample did not localize.

Fig. 15 shows contours of the deviatoric invariant of logarithmic stretches at the point of initial localization. Again, the horizontal slices (Fig. 15b) are 90° rotated relative to the solid volume (Fig. 15a) for better visualization. Comparing Figs. 14 and 15, the solutions clearly correlated regions in the specimen where the determinant function vanished for the first time with regions where the deviatoric strains were most intense (a 'blue' determinant region correlates with a 'red' deviatoric strain region, etc.). In contrast, Fig. 16 shows contours of the volumetric invariant of logarithmic stretches resembling the initial specific volume profile of Fig. 10. In general, these observations are similar to those observed for the plane strain example. For completeness, Fig. 17 shows the deformed FE mesh for the heterogeneous sample at the instant of initial localization, suggesting that the specimen moved laterally as well as twisted torsionally. Note once again that this non-uniform deformation was triggered by the imposed initial density variation alone.

Finally, Fig. 18 shows the convergence profiles of global Newton iterations for the full 3D finite deformation simulation of a heterogeneous specimen with B-bar integration. The iterations converged quadratically in all cases, suggesting optimal performance. We emphasize that all of the results presented above only pertain to the prediction of when and where a potential shear band will emerge. We have not pursued the simulations beyond the point of bifurcation due to mesh

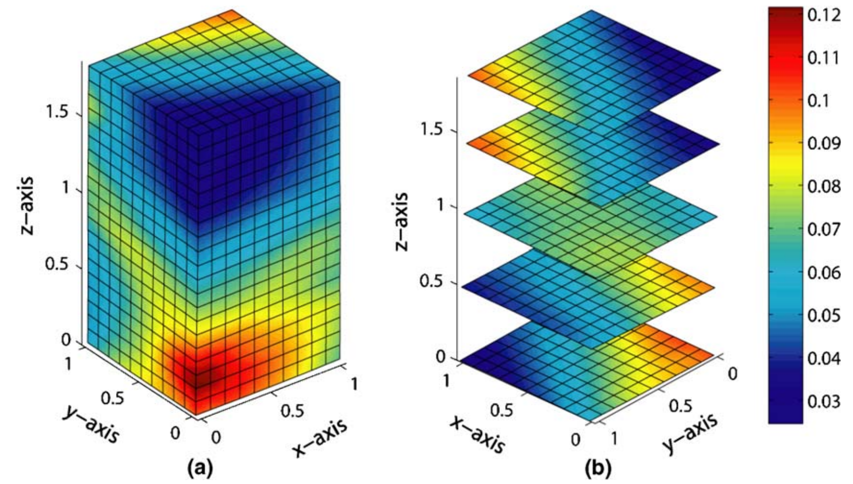

Fig. 15. Deviatoric invariant of logarithmic stretches at onset of strain localization.

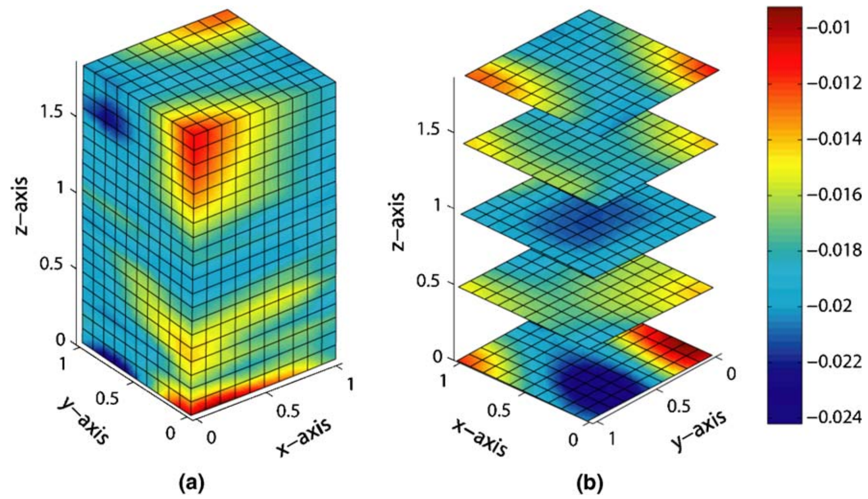

Fig. 16. Volumetric invariant of logarithmic stretches at onset of strain localization.

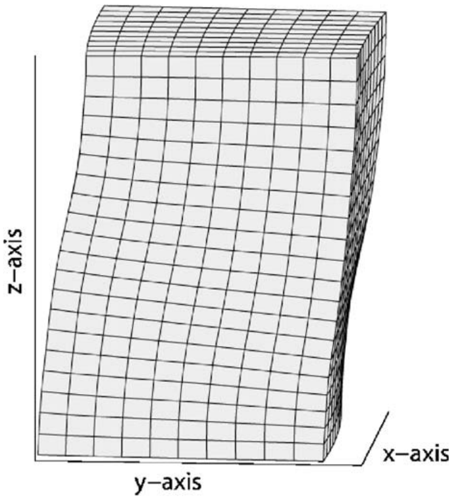

Fig. 17. Deformed finite element mesh at onset of strain localization (deformation magnified by a factor of 3).

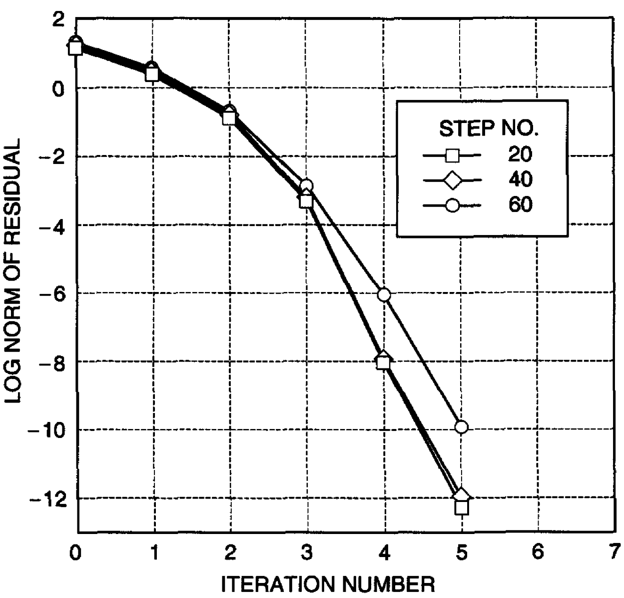

Fig. 18. Convergence profiles of global Newton iterations: finite deformation simulation of heterogeneous specimen with B-bar.

sensitivity issues inherent in rate-independent classical plasticity models in the post-localized regime. A host of regularization techniques either in the constitutive description or finite element solution are available and should be used to advance the solution to this regime.

5. Closure

We have presented a meso-scale finite element modeling approach for capturing deformation and strain localization in dense granular materials using critical state plasticity theory and nonlinear finite element analysis. This approach has been motivated in large part by recent trends in geotechnical laboratory testing allowing accurate quantitative measurement of the spatial density variation in discrete granular materials. The meso-scale approach provides a more realistic mathematical representation of imperfection; hence, it is expected to provide a more thorough capture of the deformation and strain localization processes in these materials. Potential extensions of the studies include a three-invariant enhancement of the plasticity model and application of the model to unstructured random density fields (in contrast to the structured density fields simulated in this paper). These aspects will be reported upon in a future publication.

Acknowledgements

This work has been supported by National Science Foundation under Grant Nos. CMS-0201317 and CMS-0324674 to Stanford University. We thank Professor Jack Baker of Stanford University for his assistance in generating the initial specific volume profiles used in the numerical examples, and Professor Amy Rechenmacher of USC for providing the X-Ray CT image shown in Fig. 1. We also thank the two anonymous reviewers for their constructive reviews.

References

[1] K.A. Alshibli, S. Sture, N.C. Costes, M.L. Frank, F.R. Lankton, S.N. Batiste, R.A. Swanson, Assessment of localized deformations in sand using X-ray computed tomography, Geotech. Test. J. 23 (2000) 274–299.
[2] K.A. Alshibli, S. Sture, Shear band formation in plane strain compression, J. Geotech. Geoenviron. Engrg. 126 (2000) 495–503.
[3] K.A. Alshibli, S.N. Batiste, S. Sture, Strain localization in sand: plane strain versus triaxial compression, J. Geotech. Geoenviron. Engrg. 129 (2003) 483–494.
[4] J. Desrues, R. Chambon, M. Mokni, F. Mazerolle, Void ratio evolution inside shear bands in triaxial sand specimens studied by computed tomography, Géotechnique 46 (1996) 527–546.
[5] J. Desrues, G. Viggiani, Strain localization in sand: an overview of the experimental results obtained in Grenoble using stereophotogrammetry, Int. J. Numer. Analyt. Methods Geomech. 28 (2004) 279–321.
[6] R.J. Finno, W.W. Harris, M.A. Mooney, Strain localization and undrained steady state of sands, J. Geotech. Engrg. ASCE 122 (1996) 462–473.
[7] G. Gudehus, K. Nübel, Evolution of shear bands in sand, Géotechnique 54 (2004) 187–201.
[8] A.L. Rechenmacher, R.J. Finno, Digital image correlation to evaluate shear banding in dilative sands, Geotech. Test. J. 27 (2004) 13–22.
[9] A.L. Rechenmacher, R.J. Finno, Shear band displacements and void ratio evolution to critical state in dilative sands, in: J.F. Labuz, A. Drescher (Eds.), Bifurcations & Instabilities in Geomechanics, A.A. Blakema Publishers, Lisse, 2003, pp. 193–206.
[10] I. Vardoulakis, M. Goldscheider, G. Gudehus, Formation of shear bands in sand bodies as a bifurcation problem, Int. J. Numer. Analyt. Methods Geomech. 2 (1978) 99–128.
[11] I. Vardoulakis, B. Graf, Calibration of constitutive models for granular materials using data from biaxial experiments, Géotechnique 35 (1985) 299–317.
[12] E. Bauer, W. Wu, W. Huang, Influence of an initially transverse isotropy on shear banding in granular materials, in: J.F. Labuz, A. Drescher (Eds.), Bifurcations & Instabilities in Geomechanics, A.A. Balkema, Lisse, 2003, pp. 161–172.
[13] R.I. Borja, T.Y. Lai, Propagation of localization instability under active and passive loading, J. Geotech. Geoenviron. Engrg. ASCE 128 (2002) 64–75.
[14] R. Chambon, J.-C. Moullet, Uniqueness studies in boundary value problems involving some second gradient models, Comput. Methods Appl. Mech. Engrg. 193 (2004) 2771–2796.
[15] R. Chambon, D. Caillerie, C. Tamagnini, A strain space gradient plasticity theory for finite strain, Comput. Methods Appl. Mech. Engrg. 193 (2004) 2797–2826.
[16] F. Darve, G. Servant, F. Laouafa, H.D.V. Khoa, Failure in geomaterials: continuous and discrete analyses, Comput. Methods Appl. Mech. Engrg. 193 (2004) 3057–3085.
[17] R. de Borst, H.-B. Mühlhaus, Gradient-dependent plasticity: formulation and algorithmic aspects, Int. J. Numer. Methods Engrg. 35 (1992) 521–539.
[18] A. Gajo, D. Bigoni, D. Muir Wood, Stress induced elastic anisotropy and strain localisation in sand, in: H.-B. Mühlhaus, A. Dyskin, E. Pasternak (Eds.), Bifurcation and Localisation Theory in Geomechanics, A.A. Balkema, Lisse, 2001, pp. 37–44.
[19] S. Kimoto, F. Oka, Y. Higo, Strain localization analysis of elasto-viscoplastic soil considering structural degradation, Comput. Methods Appl. Mech. Engrg. 193 (2004) 2845–2866.
[20] P.A. Klerck, E.J. Sellers, D.R.J. Owen, Discrete fracture in quasi-brittle materials under compressive and tensile stress states, Comput. Methods Appl. Mech. Engrg. 193 (2004) 3035–3056.
[21] B. Muhunthan, O. Alhattamleh, H.M. Zbib, Modeling of localization in granular materials: effect of porosity and particle size, in: J.F. Labuz, A. Drescher (Eds.), Bifurcations & Instabilities in Geomechanics, A.A. Balkema, Lisse, 2003, pp. 121–131.
[22] K. Nübel, W. Huang, A study of localized deformation pattern in granular media, Comput. Methods Appl. Mech. Engrg. 193 (2004) 2719–2743.

[23] E. Oñate, J. Rojek, Combination of discrete element and finite element methods for dynamic analysis of geomechanics problems, Comput. Methods Appl. Mech. Engrg. 193 (2004) 3087–3128.

[24] M. Ortiz, A. Pandolfi, A variational Cam-Clay theory of plasticity, Comput. Methods Appl. Mech. Engrg. 193 (2004) 2645–2666.

[25] M.R. Salari, S. Saeb, K.J. Willam, S.J. Patchet, R.C. Carrasco, A coupled elastoplastic damage model for geomaterials, Comput. Methods Appl. Mech. Engrg. 193 (2004) 2625–2643.

[26] J. Tejchman, G. Gudehus, Shearing of a narrow granular layer with polar quantities, Int. J. Numer. Analyt. Methods Geomech. 25 (2001) 1–28.

[27] I. Vardoulakis, E. Vairaktaris, E. Papamichos, Subsidence diffusion–convection: I. The direct problem, Comput. Methods Appl. Mech. Engrg. 193 (2004) 2745–2760.

[28] R.G. Wan, P.J. Guo, Constitutive modelling of granular materials with focus to microstructure and its effect on strain localization, in: J.F. Labuz, A. Drescher (Eds.), Bifurcations & Instabilities in Geomechanics, A.A. Balkema, Lisse, 2003, pp. 149–160.

[29] Z.Q. Yue, S. Chen, L.G. Tham, Finite element modeling of geomaterials using digital image processing, Comput. Geotech. 30 (2003) 375–397.

[30] K.H. Roscoe, J.H. Burland, On the generalized stress–strain behavior of 'wet' clay, in: J. Heyman, F.A. Leckie (Eds.), Engineering Plasticity, Cambridge University Press, Cambridge, 1968, pp. 535–609.

[31] A. Schofield, P. Wroth, Critical State Soil Mechanics, McGraw-Hill, New York, 1968.

[32] R.I. Borja, S.R. Lee, Cam-Clay plasticity, Part I: Implicit integration of elasto-plastic constitutive relations, Comput. Methods Appl. Mech. Engrg. 78 (1990) 49–72.

[33] R.I. Borja, Cam-Clay plasticity, Part II: Implicit integration of constitutive equation based on a nonlinear elastic stress predictor, Comput. Methods Appl. Mech. Engrg. 88 (1991) 225–240.

[34] R.I. Borja, C. Tamagnini, Cam-Clay plasticity, Part III: Extension of the infinitesimal model to include finite strains, Comput. Methods Appl. Mech. Engrg. 155 (1998) 73–95.

[35] D. Peric, M.A. Ayari, Influence of Lode's angle on the pore pressure generation in soils, Int. J. Plast. 18 (2002) 1039–1059.

[36] D. Peric, M.A. Ayari, On the analytical solutions for the three-invariant Cam clay model, Int. J. Plast. 18 (2002) 1061–1082.

[37] K. Been, M.G. Jefferies, A state parameter for sands, Géotechnique 35 (1985) 99–112.

[38] M.G. Jefferies, Nor-Sand: a simple critical state model for sand, Géotechnique 43 (1993) 91–103.

[39] M.T. Manzari, Y.F. Dafalias, A critical state two-surface plasticity model for sands, Géotechnique 47 (1997) 255–272.

[40] K. Ishihara, F. Tatsuoka, S. Yasuda, Undrained deformation and liquefaction of sand under cyclic stresses, Soils Found. 15 (1975) 29–44.

[41] S.L. Kramer, Geotechnical Earthquake Engineering, Prentice-Hall, New Jersey, 1996.

[42] A. Gens, D.M. Potts, Critical state models in computational geomechanics, Eng. Comput. 5 (1988) 178–197.

[43] R.J. Jardine, D.M. Potts, A.B. Fourie, J.B. Burland, Studies of the influence of non-linear stress–strain characteristics in soil–structure interaction, Géotechnique 36 (1986) 377–396.

[44] G.T. Houlsby, The use of a variable shear modulus in elastic–plastic models for clays, Comput. Geotech. 1 (1985) 3–13.

[45] P.V. Lade, Static instability and liquefaction of loose fine sandy slopes, J. Geotech. Engrg. ASCE 118 (1992) 51–71.

[46] R.I. Borja, K.M. Sama, P.F. Sanz, On the numerical integration of three-invariant elastoplastic constitutive models, Comput. Methods Appl. Mech. Engrg. 192 (2003) 1227–1258.

[47] J.C. Simo, T.J.R. Hughes, Computational Inelasticity, Springer-Verlag, New York, NY, 1998.

[48] J. Sulem, I. Vardoulakis, E. Papamichos, A. Oulahna, J. Tronvoll, Elasto-plastic modelling of Red Wildmoor sandstone, Mech. Cohes.-Frict. Mater. 4 (1999) 215–245.

[49] R.I. Borja, A. Aydin, Computational modeling of deformation bands in granular media, I. Geological and mathematical framework, Comput. Methods Appl. Mech. Engrg. 193 (2004) 2667–2698.

[50] R.I. Borja, Computational modeling of deformation bands in granular media, II. Numerical simulations, Comput. Methods Appl. Mech. Engrg. 193 (2004) 2699–2718.

[51] E.H. Lee, Elastic–plastic deformation at finite strains, J. Appl. Mech. (1969) 1–6.

[52] L.E. Malvern, Introduction to the Mechanics of a Continuous Medium, Prentice-Hall, Englewood Cliffs, NJ, 1969.

[53] J.E. Marsden, T.J.R. Hughes, Mathematical Theory of Elasticity, Dover Publications, New York, NY, 1983.

[54] J.C. Simo, Algorithms for static and dynamic multiplicative plasticity that preserve the classical return mapping schemes of the infinitesimal theory, Comput. Methods Appl. Mech. Engrg. 99 (1992) 61–112.

[55] Y.F. Dafalias, Plastic spin: necessity or redundancy? Int. J. Plast. 14 (1998) 909–931.

[56] R.I. Borja, Bifurcation of elastoplastic solids to shear band mode at finite strain, Comput. Methods Appl. Mech. Engrg. 191 (2002) 5287–5314.

[57] J.W. Rudnicki, J.R. Rice, Conditions for the localization of deformation in pressure-sensitive dilatant materials, J. Mech. Phys. Solids 23 (1975) 371–394.

[58] T.J.R. Hughes, The Finite Element Method, Prentice-Hall, Englewood Cliffs, NJ, 1987.

[59] J.C. Nagtegaal, D.M. Parks, J.R. Rice, On numerically accurate finite element solutions in the fully plastic range, Comput. Methods Appl. Mech. Engrg. 4 (1974) 153–177.

[60] J.C. Simo, R.L. Taylor, K.S. Pister, Variational and projection methods for the volume constraint in finite deformation elasto-plasticity, Comput. Methods Appl. Mech. Engrg. 51 (1985) 177–208.